ECOLE
POLYTECHNIQUE
DE BRUXELLES

ULB

UNIVERSITÉ LIBRE DE BRUXELLES

Study of the JUNO experiment sensitivity to the determination of the neutrino mass ordering when observing neutrino signals from core-collapse supernovae

Mémoire présenté en vue de l'obtention du diplôme
d'Ingénieur Civil Physicien

Théo Guide

Directeur
Professeur Nicolas Pauly

Co-Promoteur
Professeur Barbara Clerbaux

Superviseur
Dr. Marta Colomer Molla
Pierre-Alexandre Petitjean

Service
Métrologie Nucléaire

Année académique
2022 - 2023

UNIVERSITÉ LIBRE DE BRUXELLES

UNIVERSITÉ LIBRE DE BRUXELLES

Exemplaire à apposer sur le mémoire ou travail de fin d'études,
au verso de la première page de couverture.

Réservé au secrétariat :	**Mémoire réussi***	**OUI**
NON		

CONSULTATION DU MEMOIRE/TRAVAIL DE FIN D'ETUDES

Je soussigné

NOM :
Guide ……………………………………………………………………………
………………………

PRENOM :
Théo ……………………………………………………………………………
………………..

TITRE du travail :
Study of the JUNO experiment sensitivity to the determination
of the neutrino mass ordering when observing neutrino
signals from core-collapse supernovae
……………………………………………………………………………
…………………………………

AUTORISE*

~~**REFUSE***~~

la consultation du présent mémoire/travail de fin d'études par les utilisateurs des bibliothèques de l'Université libre de Bruxelles.

Si la consultation est autorisée, le soussigné concède par la présente à l'Université libre de Bruxelles, pour toute la durée légale de protection de l'œuvre, une licence gratuite et non exclusive de reproduction et de communication au public de son œuvre précisée ci-dessus, sur supports graphiques ou électroniques, afin d'en permettre la consultation par les utilisateurs des bibliothèques de l'ULB et d'autres institutions dans les limites du prêt inter-bibliothèques.

** Biffer la mention inutile*

Fait en deux exemplaires, **Bruxelles, le** 20/08/23

Signature

Guide

** Biffer la mention inutile*

Formulaire version 04/2015

Abstract

Théo Guide

Master of Science in Physics Engineering

Université Libre de Bruxelles - École Polytechnique de Bruxelles

2022-2023

Study of the JUNO experiment sensitivity to the determination of the neutrino mass ordering when observing neutrino signals from core-collapse supernovae

Ever since neutrinos have been confirmed to be massive particles, a lot of physics exeperiments have been aimed towards the determination of the neutrino mass ordering (NMO). In this context, this work investigates how sensitive the JUNO experiment is to the determination of the NMO when observing neutrino signals from a core-collapse supernova (CCSN). This work uses the CCSN numerical model developed by the Garching group, based on the Lattimer- Swesty and Shen equations of state, to generate time spectra of the number of events recorded in JUNO called lightcurves. A Poisson likelihood ratio test is constructed to introduce two statistical methods, the Asimov and toy Monte Carlo pseudo-experiment methods, which take into account the uncertainty about the bounce time of the CCSN through a specific χ^2 test and are used on the lightcurves to determine how sensitive JUNO is to the determination of the NMO based on CCSN observations. The impact of the CCSN distance, mass, model, the interaction channels and the time window on both the lightcurves and the statistical tests are assessed as well. Based on the benchmark scenario of a 27 $M_\odot$ CCSN at 10 kpc described by the Shen EoS, the Asimov method reports an NMO determination sensitivity of 2.95 σ in the inverse mass ordering case and 2.75 σ in the normal mass ordering case. The toy Monte Carlo method reports mixed results based on how it is defined, when the uncertainty about the bounce time fluctuates for each pseudo-experiment the results are inconclusive but when it is determined beforehand and fixed for all pseudo-experiments, it shows results comparable to those of the Asimov method.

Keywords: neutrino mass ordering, core-collapse supernovae, JUNO, Poisson-χ^2 likelihood, Asimov method, toy Monte Carlo experiments.

Acknowledgements

I would first like to express my sincere gratitude to Prof. Barbara Clerbaux. From the first day to the last, she has been a constant source of advice, expertise and encouragement. It was a pleasure to work under her supervision.

Next, I want to thank Prof. Nicolas Pauly for giving me the opportunity to take this master thesis, for his insightful comments and enthusiasm towards the direction this work eventually took.

This thesis would not have been possible without the help of my supervisors Pierre-Alexandre Petitjean and Dr. Marta Collomer Molla. I would like to thank Pierre-Alexandre for his advice, availability and for pushing me in the right direction when it was needed. And last but certainly not least, I would like to acknowledge Dr. Marta Colomer Molla for her tireless availability, patience and guidance throughout this whole year.

Contents

Introduction

Neutrinos are mysterious particles. Since their discovery, they have for a long period of time been thought to have no mass. It took the observation of a discrepancy between the expected and measured solar neutrino flux at various experiments in the 1970's to explore the possibility of the neutrino oscillation phenomenon [1], initially proposed by Bruno Pontecorvo in the late 1950's [2], which necessarily implies massive neutrinos. The eventual observation of neutrino oscillations by Takaaki Kajita & Arthur B. McDonald won them the Nobel Prize in 2015 [3].

As previous experiments were designed to measure the mass difference between the neutrinos of different flavors, rather than the absolute mass, a lot of physics experiments have been proposed to determine the neutrino mass ordering. In this context the JUNO experiment emerged.

The Jiangmen underground neutrino observatory (JUNO) is a medium baseline liquid scintillator neutrino detector in China, buried 700 m underground and at equal distance ($\sim$ 52km) of two nuclear powerplants, which aims to determine the neutrino mass ordering over 6 years of data taking by observing the reactor $\bar{\nu}_e$ energy spectrum with an excellent energy resolution [4]. However, JUNO is not sensitive to only nuclear reactor $\bar{\nu}_e$, it is also sensitive to other neutrino sources to be able to measure other parameters than the neutrino mass ordering. The neutrino sources JUNO is sensitive to include core-collapse supernovae (CCSN), which from a neutrino observation point of view are very interesting phenomena as they emit 99% of their energy in the form of neutrinos in all flavors.

As predicted by state of the art numerical models, the time spectra of CCSN neutrinos contain information about the neutrino mass ordering. It should thus be possible by using the right statistical fitting tests to draw conclusions on the neutrino mass ordering when observing a single CCSN, as opposed to the 6 years of data taking for the reactor $\bar{\nu}_e$.

This work chooses to investigate this exact hypothesis. By computing the expected time spectra of the CCSN and constructing the appropriate statistical tests the global objective is to compute the expected sensitivity of JUNO to the NMO determination.

The master thesis begins by putting the neutrinos in the context of the standard model and listing the current knowledge on neutrino parameters in Chapter 1. Next, the CCSN phenomenon is analysed from a neutrino-emission point of view in Chapter 2 and afterwards the JUNO experiment and its measurement mechanisms are presented in Chapter 3.

The CCSN time spectra as measured in JUNO are then defined and computed in Chapter 4, then the statistical tests of interest for the NMO discrimination are constructed in Chapter 5 and finally the expected sensitivity of the JUNO experiment is computed based on the expected time spectra and statistical tests in Chapter 6.

Chapter 1

The Standard Model & neutrinos

This chapter begins with a brief description of the Standard Model followed afterwards by a more extensive description of the role neutrinos play in it. It then proposes a complete theoretical discussion of the neutrino oscillation phenomenon and finally the chapter concludes by summarizing the current state of knowledge on neutrino parameters and ongoing experiments aiming to resolve open questions.

1.1 The Standard Model of particle physics

The Standard Model (SM) is the theory currently accepted to be the most fundamental description of the Universe, containing the description of elementary particles on one hand and of three of the four fundamental interactions on the other. Simply put, the SM offers a unifying formalism for particles and interactions, describing interactions as matter particles (fermions) exchanging virtual particles (bosons), which are the quantization of the underlying interaction-specific quantum field. The considered interactions in the SM are the strong interaction, the weak interaction and the electromagnetic interaction; the gravitational interaction has yet to be described by the SM on a subatomic level.

The current classification, and by extent our total knowledge, of the elementary particles constituting the SM is represented in Fig. 1.1.

On one hand, the SM describes the fundamental components of matter via the spin-$\frac{1}{2}$ particles called fermions, which are divided into two categories : leptons and quarks. The leptons as described by the SM are either charged and massive or neutral and massless, the latter are called neutrinos. There are 6 types, called flavors, of quarks, with all varying masses and an electric charge of either $\frac{2}{3}$ or $\frac{-1}{3}$.

The fermions as a whole are divided into three families, each represented by one flavor. The first family consists of the up (u) and down (d) quarks, the electron (e^-) and the electron neutrino (ν_e), the second family of the charm (c) and strange (s) quarks, the muon (μ) and the muon neutrino (ν_μ) and finally the third family regroups the top (t) and bottom (b) quarks, the tau (τ) and the tau neutrino (ν_τ).

Twelve fermions, and its corresponding antiparticles with same mass, spin and opposite charges, are thus predicted by the SM to constitute matter. *Stable* matter, however, is made up solely of the fermions of the first family, the electron neutrino excluded.

The up and down quark bind together through the strong interaction to make up neutrons (udd) and protons (uud) and together with the electron make up all possible atoms.

On the other hand, the SM describes the three fundamental interactions through particles called Gauge bosons. As such, when fermions interact with each other they do so by virtually exchanging one of the four gauge bosons associated to a quantum field, in turn associated to the corresponding force at stake. Thus, a Gauge boson is mediating each of the three interactions described by the SM: the electromagnetic interaction is mediated by the neutral and massless photons γ, the strong interaction by the neutral and massless gluons (g), and the weak interaction by the massive Z and $W^{\pm}$ bosons, respectively neutral and charged. Bosons are fundamentally different from fermions as they notably have integer spins.

Lastly, the SM contains a 5$^{\text{th}}$ force carrier : the Higgs boson. Theorized in the 1960's, presumably detected in 2012 and confirmed to have been detected in 2013 [5], the Higgs boson is a scalar boson with neutral charge and spin 0. Elementary particles get their mass from their permanent interaction with the Higgs field, which is mediated by the so-called Higgs boson.

This master thesis focuses on neutrinos and the assessment of their unknown parameters. As explained above, the SM predicts massless neutrinos. However, it is now known through the observation of the neutrino oscillation phenomenon that neutrinos have a non-zero mass. The SM is consequently not complete and a physical model beyond the SM, or a correction of the latter, needs to be formalized in order to theoretically explain the massive neutrinos in the SM formalism.

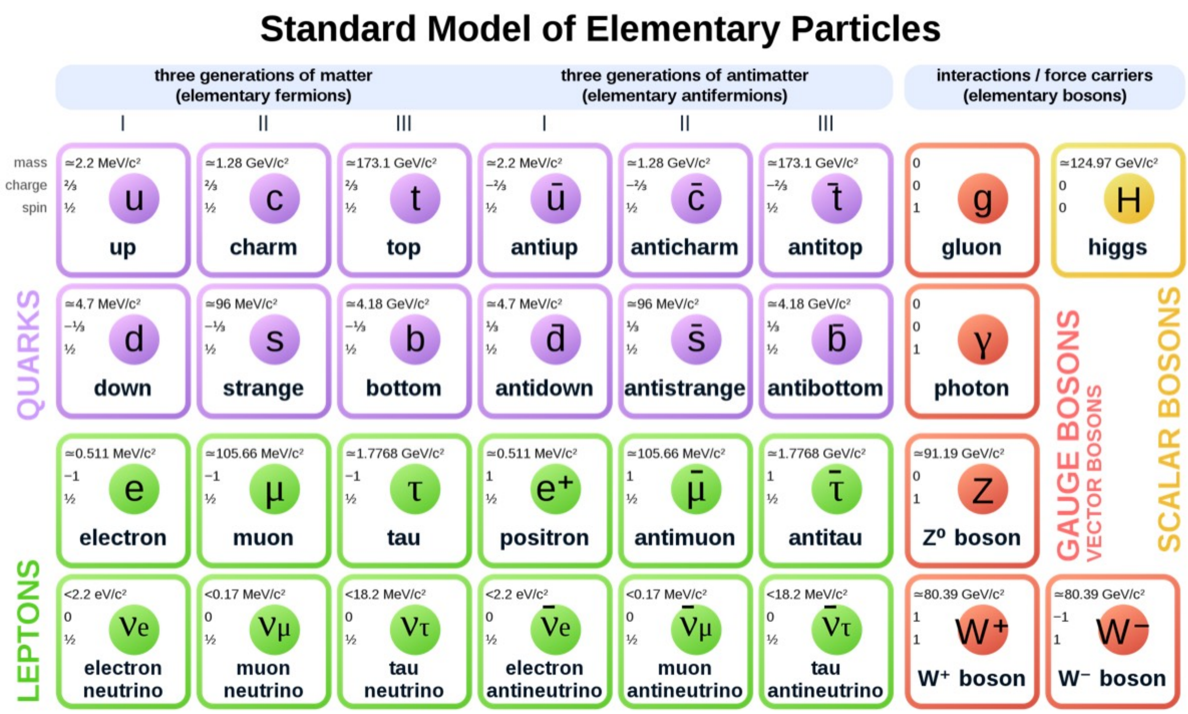

Figure 1.1: The Standard Model of elementary particles with explicit antimatter [6]

1.2 Neutrino physics

1.2.1 The weak interaction

Neutrinos are unique particles as they are sensitive to only the weakest of the three interactions described by the SM : the weak interaction. The weak interaction is mediated through the Z and $W^{\pm}$ bosons and can be divided into two types of interactions: neutral current (NC), when a Z is exchanged and no charges, and charged current (CC) if a $W^{\pm}$ is the mediator.

Neutral current reactions, in the context of neutrinos, can be thought of as elastic scattering reactions mediated by the exchange between both fermions of the Z boson, which is neutral as expected by the reaction not involving some charge modification. For example the $\nu - p$ and $\nu - e^-$ elastic scattering reactions

$$\nu + p \xrightarrow{Z} \nu + p \quad (1.1) \qquad\qquad \nu + e^- \xrightarrow{Z} \nu + e^- \quad (1.2)$$

Charged current interactions on the other hand are reactions involving nuclear decays. These reactions are mediated by a charged boson, either W^+ or W^-. For example the beta decay reaction: it changes one of the neutron's down quark into an up quark, transforming said neutron into a proton. This process is accompanied by the emission of a virtual W^- boson which decays into an electron and an electronic anti-neutrino, respecting thereby the different conservation laws

$$d \to u + W^- \to u + e^- + \bar{\nu}_e \tag{1.3}$$

$$= \; n \to p + e^- + \bar{\nu}_e \tag{1.4}$$

1.2.2 Neutrino oscillations phenomenon

In 1970 the Homestake experiment took place, aiming to study the thermonuclear mechanism of the sun's core, namely the $p - p$ cycle (Eq. 1.5)

$$4p \to \alpha + 2e^+ + 2\nu_e \tag{1.5}$$

through the measurement of its associated neutrino flux on earth. The results of this experience showed a measured neutrino flux of about $\frac{1}{3}$ lower than the expected ν_e neutrino flux [1]. This discrepancy was the start of the *solar neutrino problem* which led to the discovery of neutrino oscillations.

Besides other experiments confirming the discrepancy of neutrino flux with respect to what the solar SM predicts [7], the solar neutrino problem took new experiments and about a couple of decades to be solved through the confirmation of the neutrino oscillation idea, loosely proposed by Bruno Pontecorvo in the late 1950's [2]. The Super-Kamiokande project in 1998 [8] and the Sudbury Neutrino Observatory in 2002 [9] set the definitive answer to the problem by specifically observing neutrino oscillations in accordance with the new and improved theoretical derivation. Leaders of both projects jointly received the Nobel Prize in Physics in 2015 for the observation of neutrino oscillations [3].

More formally, the phenomenon of neutrino oscillations can be explained through the generic quantum superposition formalism. Neutrinos are created and interact through the weak interaction in flavor (e, μ, τ) eigenstates, which are in fact a superposition of three states of definite mass (ν_1, ν_2, ν_3). As a neutrino propagates through space, the quantum phases of these three different mass states evolve at different speeds and this causes the neutrino's global mass state superposition to change over time. Since different combinations of mass states correspond to different combinations of flavor states, the changing mass states as the neutrino propagates also cause the global flavor state to change.

It is thus possible to express the neutrino flavor-eigenstates as a function of the neutrino mass-eigenstates and vice versa by means of a basis change. This change of basis, from the flavor to the mass eigenstates, can be seen as a rotation in three dimensions, characterized by 3 angles called the mixing angles. In the literature this rotation is conventionally represented the 3×3 unitary lepton mixing matrix called the PMNS (Pontecorvo-Maki-Nakagawa-Sakata) matrix

$$\begin{aligned}\mathcal{U} &= \begin{pmatrix} 1 & 0 & 0 \\ 0 & c_{23} & s_{23} \\ 0 & -s_{23} & c_{23} \end{pmatrix} \times \begin{pmatrix} c_{13} & 0 & s_{13}e^{-i\delta_{\mathrm{CP}}} \\ 0 & 1 & 0 \\ -s_{13}e^{i\delta_{\mathrm{CP}}} & 0 & c_{13} \end{pmatrix} \times \begin{pmatrix} c_{12} & s_{12} & 0 \\ -s_{12} & c_{12} & 0 \\ 0 & 0 & 1 \end{pmatrix} \\ &= \begin{pmatrix} c_{12}c_{13} & s_{12}c_{13} & s_{13}e^{-i\delta_{\mathrm{CP}}} \\ -s_{12}c_{23} - c_{12}s_{23}s_{13}e^{i\delta_{\mathrm{CP}}} & c_{12}c_{23} - s_{12}s_{23}s_{13}e^{i\delta_{\mathrm{CP}}} & s_{23}c_{13} \\ s_{12}s_{23} - c_{12}c_{23}s_{13}e^{i\delta_{\mathrm{CP}}} & -c_{12}s_{23} - s_{12}c_{23}s_{13}e^{i\delta_{\mathrm{CP}}} & c_{23}c_{13} \end{pmatrix}\end{aligned} \tag{1.6}$$

with the notation $s_{ij} = \sin(\theta_{ij})$, $c_{ij} = \cos(\theta_{ij})$. This unitary matrix is the product of three individual rotation matrices and has four parameters, the three mixing angles (θ_{12}, θ_{23}, θ_{13}) and the Dirac phase δ_{CP} linked to the possibility of neutrino oscillations violating CP symmetry, which has yet to be confirmed, and in case neutrinos are proven to be Majorana particles, this phase has to be redefined with two Majorana phases [10].

The PMNS matrix thus gives the probability of measuring a mass state i given a neutrino of flavor f by taking the square of corresponding matrix element $|\mathcal{U}_{fi}|^2$. This is consistent with the fact that summing the squared matrix elements on one row gives a unit probability, as performing a measure on an arbitrary flavored neutrino necessarily always yields one mass state $\sum_{i=1}^{3} |\mathcal{U}_{fi}|^2 = 1$.

1.3 Neutrino oscillations

Neutrinos interact in their flavor eigenstates $|\nu_f\rangle$ while they propagate in their mass eigenstates $|\nu_i\rangle$. The flavor states are a superposition of mass states $|\nu_i\rangle$ defined by the matrix elements $\mathcal{U}_{fi}$ of the PNMS matrix

$$\begin{aligned}|\nu_e\rangle &= \mathcal{U}_{e1}|\nu_1\rangle + \mathcal{U}_{e2}|\nu_2\rangle + \mathcal{U}_{e3}|\nu_3\rangle \\ |\nu_\mu\rangle &= \mathcal{U}_{\mu 1}|\nu_1\rangle + \mathcal{U}_{\mu 2}|\nu_2\rangle + \mathcal{U}_{\mu 3}|\nu_3\rangle \\ |\nu_\tau\rangle &= \mathcal{U}_{\tau 1}|\nu_1\rangle + \mathcal{U}_{\tau 2}|\nu_2\rangle + \mathcal{U}_{\tau 3}|\nu_3\rangle\end{aligned} \tag{1.7}$$

Before deriving the neutrino oscillation behaviour of the more complex three-flavor situation, it is common in the literature to first introduce the two-flavor scenario first. The two-flavor situation gives the necessary physical intuition to understand the phenomenon while keeping the calculations short, before deriving the three-flavor situation.

The approach and general development leading to the neutrino oscillation expressions in this section are taken from Pr. Barbara Clerbaux's graduate course on particle physics at the Université Libre de Bruxelles [11].

1.3.1 Two-flavor neutrino oscillations

In the two-flavor situation, a generic flavor eigenstate can be written as

$$|\nu_f\rangle = \sum_{i=1}^{2} U_{fi} |\nu_i\rangle \tag{1.8}$$

where here the electronic and muonic flavors are considered ($f = e, \mu$) and U_{fi} represents the basis change. This superposition can be understood as basis change, a 2D rotation in the flavor-mass space, defined by a rotation matrix

$$U = \begin{pmatrix} \cos\theta & \sin\theta \\ \sin\theta & \cos\theta \end{pmatrix} \tag{1.9}$$

containing here only one mixing angle θ. More explicitely, Eq. 1.8 now becomes

$$\begin{aligned} |\nu_e\rangle &= \cos\theta\,|\nu_1\rangle + \sin\theta\,|\nu_2\rangle \\ |\nu_\mu\rangle &= -\sin\theta\,|\nu_1\rangle + \cos\theta\,|\nu_2\rangle \end{aligned} \tag{1.10}$$

These mass states are each solution of the non-relativistic Schrödinger equation

$$\hat{H}\,|\nu_i\rangle = E_i\,|\nu_i\rangle = i\hbar\frac{d}{dt}\,|\nu_i\rangle \tag{1.11}$$

where E_i is the energy of mass eigenstate $|\nu_i\rangle$ or the eigenvalue of $|\nu_i\rangle$ from the Hamiltonian which can be written

$$\hat{H} = \begin{pmatrix} E_1 & 0 \\ 0 & E_2 \end{pmatrix} \tag{1.12}$$

Considering the neutrino of flavor f is produced at $t = 0$ and subsequently propagates in vacuum, the solutions of the Schrödinger equation (1.11) are the following propagating mass states

$$|\nu_i(t)\rangle = e^{\frac{-iE_it}{\hbar}}\,|\nu_i(0)\rangle \quad ,i = 1, 2 \tag{1.13}$$

To highlight neutrino oscillation, at $t = 0$ only one of the two neutrino flavor eigenstates can be observed

$$|\nu_e(0)\rangle = |1\rangle \quad ; \quad |\nu_\mu(0)\rangle = |0\rangle \tag{1.14}$$

By inverting Eq. 1.10 one obtains the following mass eigenstates at $t = 0$

$$|\nu_1(0)\rangle = \cos\theta\,|1\rangle \quad ; \quad |\nu_2(0)\rangle = \sin\theta\,|1\rangle \tag{1.15}$$

This gives the opportunity to write the time evolution for $t > 0$ of $|\nu_\mu(t)\rangle$ from Eq. 1.10 using Eq. 1.14 and Eq. 1.15:

$$\begin{aligned} |\nu_\mu(t)\rangle &= -\sin\theta\,|\nu_1(t)\rangle + \cos\theta\,|\nu_2(t)\rangle & (1.16) \\ &= -\sin\theta e^{\frac{-iE_1t}{\hbar}}\,|\nu_1(0)\rangle + \cos\theta e^{\frac{-iE_2t}{\hbar}}\,|\nu_2(0)\rangle & (1.17) \\ &= -\sin\theta e^{\frac{-iE_1t}{\hbar}}\cos\theta\,|1\rangle + \cos\theta e^{\frac{-iE_2t}{\hbar}}\sin\theta\,|1\rangle & (1.18) \\ &= \frac{1}{2}\sin(2\theta)\left(e^{\frac{-iE_2t}{\hbar}} - e^{\frac{-iE_1t}{\hbar}}\right)|1\rangle & (1.19) \end{aligned}$$

where the property $\sin(2a) = 2\sin a\cos a$ has been used to go from line (1.18) to (1.19). This time evolution allows to compute the oscillation probability, meaning the probability to measure a neutrino of flavor ν_μ after a neutrino initially created as ν_e propagates over a time t. The oscillation probability is computed through the Born rule with appropriate initial conditions Eq. 1.14 and by taking advantage of $\sin^2 a = \frac{1-\cos(2a)}{2}$:

$$
\begin{aligned}
P_{\nu_e \to \nu_\mu} = |\langle \nu_e(0)|\nu_\mu(t)\rangle|^2 &= \frac{1}{4}\sin^2(2\theta)\left|\left(e^{\frac{-iE_2t}{\hbar}} - e^{\frac{-iE_1t}{\hbar}}\right)\right|^2 && (1.20)\\
&= \frac{1}{4}\sin^2(2\theta)\left(2 - 2\cos\left(\frac{E_2-E_1}{\hbar}t\right)\right) && (1.21)\\
&= \sin^2(2\theta)\sin^2\left(\frac{E_2-E_1}{2\hbar}t\right) && (1.22)
\end{aligned}
$$

To simplify this expression, an approximation is introduced that seemingly contradicts the non-relativistic Schrödinger equation used previously, but still holds up for high-energy neutrinos [12]. The simplification consists of considering said high energy neutrinos, for which $v \sim c$, $p_1 \sim p_2 = p$ and $p \gg m_i$. This allows to write a new expression for the mass state energies E_i

$$
\begin{aligned}
&E_i^2 = (pc)^2 + (m_ic^2)^2 = c^2\left[p^2\left(1 + \frac{m_i^2c^2}{p^2}\right)\right] \approx c^2\left[p + \frac{1}{2}\frac{m_i^2c^2}{p}\right] && (1.23)\\
&\implies E_2 - E_1 \approx \frac{(m_2^2 - m_1^2)c^4}{2p} && (1.24)
\end{aligned}
$$

Which by substituting $L \approx ct$, $p = \frac{E}{c}$ with E the average energy of the neutrino and injected in Eq. 1.22 finally gives:

$$
P_{\nu_e \to \nu_\mu} = \sin^2(2\theta)\sin^2\left(\frac{(m_2^2 - m_1^2)c^3L}{4\hbar E}\right) \tag{1.25}
$$

It is common to use specific units for the variables : $[m] = \frac{\mathrm{eV}^2}{c^4}$, $[E] = \mathrm{GeV}$, $[L] = \mathrm{km}$ as to get, by injecting the numerical values of the constants:

$$
P_{\nu_e \to \nu_\mu} = \sin^2(2\theta)\sin^2\left(1.27\frac{\Delta m_{21}^2 L}{E}\right) \tag{1.26}
$$

where $\Delta m_{21}^2 = m_2^2 - m_1^2$.

The oscillation probability is thus non-zero under two conditions : the mixing angle θ must be non-zero, meaning the mass states must be different from the flavor states, and the mass difference Δm_{21}^2 must be non-zero aswell, implying mass states are different and thus at least one mass state has a mass.

For fixed values of θ, Δm_{21}^2 and neutrino energy E, the oscillation probability varies periodically with the propagation distance L between 0 and $\sin^2(2\theta)$ with a spatial period $T = \pi\frac{4\hbar E}{\Delta m_{21}^2 c^3}$. Since this is a two-flavor framework, the non-oscillation probability forms perfect destructive interferences with the oscillation probability, both survival probabilities are plotted on Fig. 1.2a.

When looking on the contrary on Fig. 1.2b at how the oscillation probability behaves in function of $\frac{E}{L}$ at fixed E, one sees that for small values of L, meaning far from the neutrino creation point, the oscillations are too fast and a mean oscillation effect will be observed. For large values of $\frac{1}{L}$, meaning close to the source, no oscillations happen.

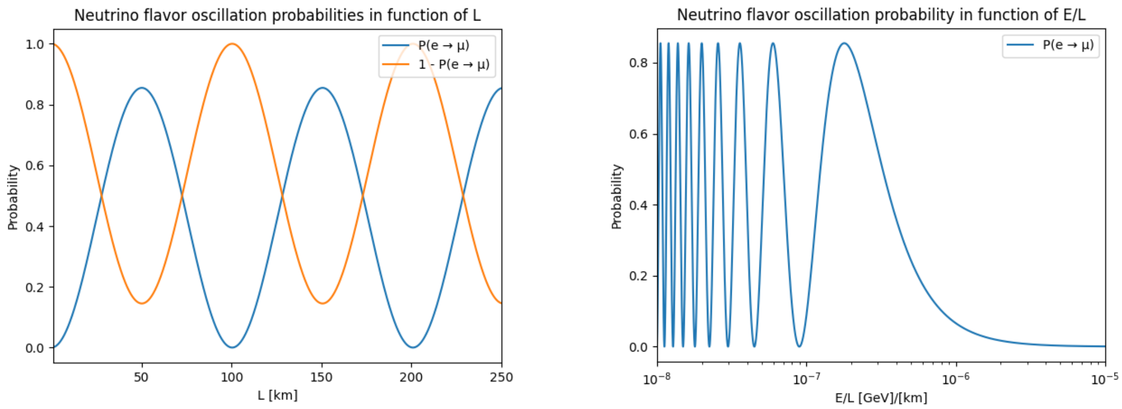

(a) $P_{\nu_e \to \nu_\mu} = f\,(L)$ and $1 - P_{\nu_e \to \nu_\mu} = f\,(L)$ (b) $P_{\nu_e \to \nu_\mu} = f\left(\frac{E}{L}\right)$

Figure 1.2: The oscillation probability of ν_e in function of the travelled distance L or its inverse. The plots' legends use a notation considering only the flavor, e.g. $P(e \to \mu) \equiv P_{\nu_e \to \nu_\mu}$, parameters are taken according to Table 1.1: $\Delta m^2_{12} = 7.39 \cdot 10^{-5}$, $\theta_{12} = 33.82$ and $E = 3 \cdot 10^{-3}$ GeV.

1.3.2 Three-flavor neutrino oscillations

The three-flavor oscillation mechanism follows the same physical intuition as the two-flavor situation, but is defined by the 3×3 PMNS matrix. Hence, the probability for a neutrino created at $t = 0$ in flavor α to oscillate to the flavor β after a propagation time t is defined by

$$P_{\nu_\alpha \to \nu_\beta} = |\, \langle \nu_\alpha(0) | \nu_\beta(t) \rangle \,|^2 = \left| \sum_{i=1}^{3} \mathcal{U}^*_{\alpha i} \mathcal{U}_{\beta i} e^{-i m_i^2 \frac{L}{2E}} \right|^2 \tag{1.27}$$

as developed in [13]. It is interesting to compute the survival probability of a neutrino, as that is the quantity that will have an imprint on the data observed by neutrino experiments like JUNO. Let's consider the survival probability of a ν_e over a propagation $L = ct$ assuming the normal mass hierarchy and using the same unit system as for Eq. 1.26

$$P_{\nu_e \to \nu_e} = \left| \sum_{i=1}^{3} \mathcal{U}^*_{ei} \mathcal{U}_{ei} e^{-i m_i^2 \frac{L}{2e}} \right|^2 \tag{1.28}$$

$$= 1 - \sin^2(2\theta_{12}) \cos^4\theta_{13} \sin^2\left(1.27 \frac{\Delta m^2_{21} L}{E}\right)$$
$$- \sin^2(2\theta_{13}) \left[\cos^2\theta_{12} \sin^2\left(1.27 \frac{\Delta m^2_{31} L}{E}\right) + \sin^2\theta_{12} \sin^2\left(1.27 \frac{\Delta m^2_{32} L}{E}\right) \right] \tag{1.29}$$

The survival probability is, besides of E and L, function of the different squared mass differences. It is known from neutrino parameters measurements (cf. section 1.4) that $\Delta m^2_{21} \ll \Delta m^2_{32}, \Delta m^2_{31}$ which allows to write the survival probability in terms of a fast oscillation $\Delta m^2_{32} \approx \Delta m^2_{31} = \Delta m^2_{\text{fast}}$ and a slow oscillation Δm^2_{12}. This leads to the new survival probability

$$P_{\nu_e \to \nu_e} \approx 1 - \sin^2(2\theta_{12}) \cos^4\theta_{13} \sin^2\left(1.27 \frac{\Delta m^2_{21} L}{E}\right) - \sin^2(2\theta_{13}) \sin^2\left(1.27 \frac{\Delta m^2_{\text{fast}} L}{E}\right) \tag{1.30}$$

$$= 1 - P_{\text{slow}} - P_{\text{fast}} \tag{1.31}$$

This survival probability depends on the two squared mass differences. The θ_{23} mixing angle and mass splitting terms are typically measured by atmospheric neutrino experiments, while θ_{12} and Δm^2_{12} are determined with the solar neutrino neutrino data [13].

These slow and fast components smoothly add up as can be seen on Fig. 1.3 where the high frequency sine of the atmospheric oscillations is weighted by the low frequency sine of the fast solar oscillations.

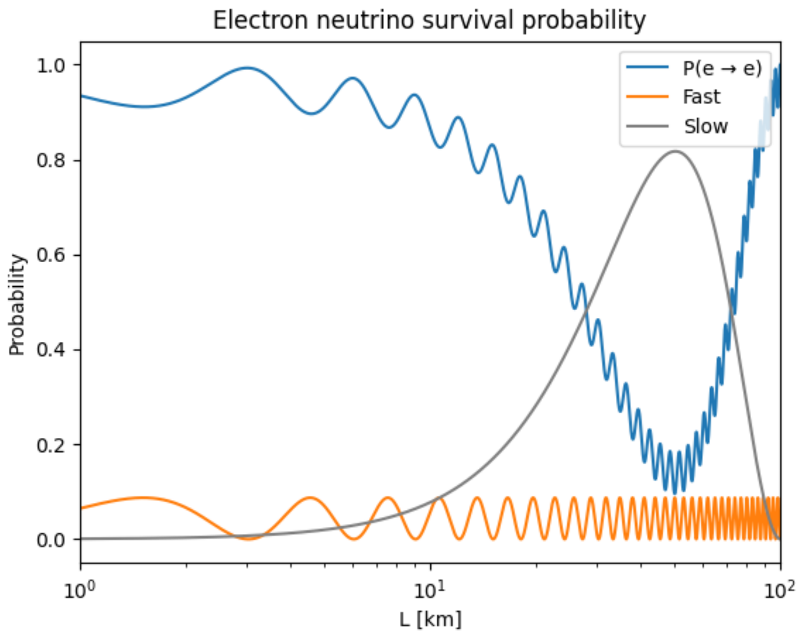

Figure 1.3: Electron neutrino survival probability in the three-flavor framework, considering $\Delta m^2_{32} \approx \Delta m^2_{31} = \Delta m^2_{\text{fast}}$. The plot's legend uses the same notation as in Fig. 1.2, parameters are taken according to Table 1.1 and $E = 3 \cdot 10^{-3}$ GeV.

1.4 Neutrino parameters: state of knowledge

1.4.1 Neutrino mass ordering

As only the values of Δm^2_{ij} can be assessed via neutrino oscillations, the ordering of the mass eigenstates remains unkown. In fact, when defining $m_2 > m_1$ as a fixed parameter, it is still not known whether neutrinos follow a normal mass ordering (NO) $m_3 > m_2 > m_1$ or an inverted mass ordering (IO) $m_3 < m_1 < m_2$. This is the neutrino mass ordering (NMO) problem.

Fig. 1.4 gives a representation of each mass state, in the NO and IO situation, with their respective flavor content. The flavor content f of a mass state i is computed via the PNMS matrix : $|\mathcal{U}_{fi}|^2$

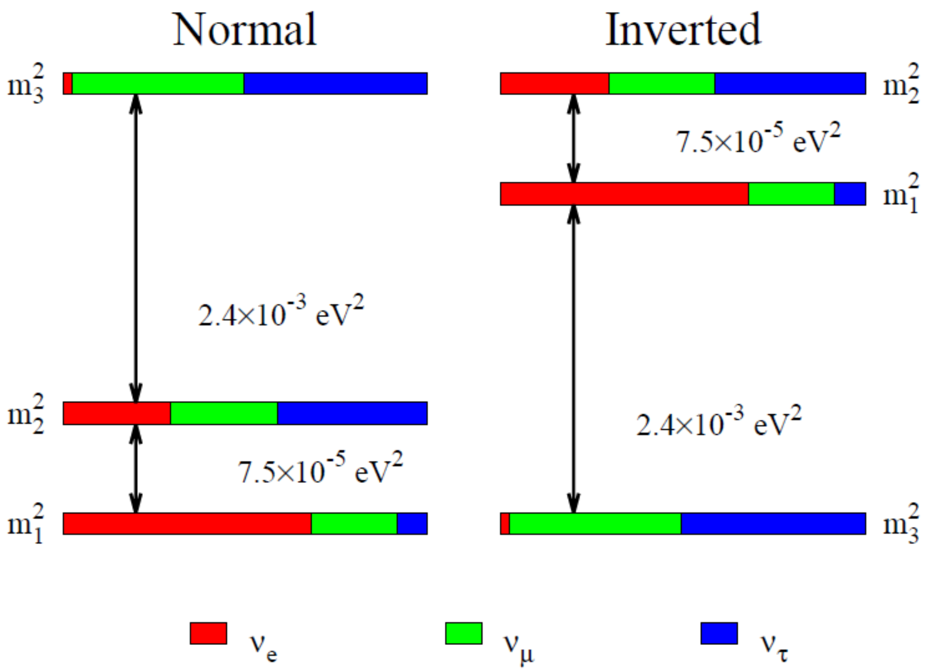

Figure 1.4: Representation of the possible neutrino mass orderings with the flavor content of each mass state represented by the coloring of the mass state bars [13]. Numerical values are a bit outdated.

The squared mass differences thus depend on the ordering, from which they get their sign:

$$\begin{array}{lcll}
\Delta m^2_{21} = m^2_2 - m^2_1 & \Longrightarrow & \Delta m^2_{21} > 0, & \forall\,\mathrm{NMO} \\
\Delta m^2_{32} = m^2_3 - m^2_2 & \Longrightarrow & \Delta m^2_{32} > 0, & \mathrm{NMO} = \mathrm{NO} \\
 & & \Delta m^2_{32} < 0, & \mathrm{NMO} = \mathrm{IO} \\
\Delta m^2_{31} = m^2_3 - m^2_1 & \Longrightarrow & \Delta m^2_{31} > 0, & \mathrm{NMO} = \mathrm{NO} \\
 & & \Delta m^2_{31} < 0, & \mathrm{NMO} = \mathrm{IO}
\end{array}$$

1.4.2 Neutrino oscillation parameters

Neutrinos are currently still at the source of many research projects, of both theoretical and experimental nature. On the experimental side, a very prolific domain consists of accurately measuring the neutrino oscillation parameters θ_{ij} and Δm^2_{ji}.

The Super-Kamiokande experiments for example are sensitive to the atmospheric neutrino oscillations parameters $\Delta m^2_{13}, \theta_{13}$ [14], while other experiments such as the Borexino experiment focus on the solar oscillation parameters $\Delta m^2_{12}, \theta_{12}$ [15] .

The particle data group regroups all current experimental knowledge on particle physics with adapted confidence intervals, over all validated experiments. The up-to-date neutrino oscillation parameters are listed in Table 1.1 [16]. There is still a relatively big uncertainty on the value of θ_{23}, making its accurate measurement a big challenge for ongoing and upcoming experiments.

Using the values in Table 1.1, assuming normal mass ordering, a null charge-parity (CP) violating phase $\delta_{\mathrm{CP}} = 0$ and considering the central values of the 3σ intervals gives

[1] $\Delta m^2_{32} + \Delta m^2_{21} = m^2_3 - m^2_2 + m^2_2 - m^2_1 = m^2_3 - m^2_1 = \Delta m^2_{31}$

Parameter	Best fit	3σ interval
NO		
Δm^2_{21} [eV^2]	7.39×10^{-5}	$6.79 \rightarrow 8.01$
Δm^2_{32} [eV^2]	2.449×10^{-3}	$2.358 \rightarrow 2.554$
$\sin^2(\theta_{12})$	0.310	$0.275 \rightarrow 0.350$
$\sin^2(\theta_{23})$	0.558	$0.427 \rightarrow 0.609$
$\sin^2(\theta_{13})$	0.02241	$0.02046 \rightarrow 0.02440$
θ_{12} [°]	33.82	$31.61 \rightarrow 36.27$
θ_{23} [°]	48.3	$40.8 \rightarrow 51.3$
θ_{13} [°]	8.61	$8.22 \rightarrow 8.99$
IO		
Δm^2_{21} [eV^2]	7.39×10^{-5}	$6.79 \rightarrow 8.01$
Δm^2_{32} [eV^2]	-2.509×10^{-3}	$-2.603 \rightarrow -2.416$
$\sin^2(\theta_{12})$	0.310	$0.275 \rightarrow 0.350$
$\sin^2(\theta_{23})$	0.563	$0.430 \rightarrow 0.612$
$\sin^2(\theta_{13})$	0.02261	$0.02066 \rightarrow 0.02461$
θ_{12} [°]	33.82	$31.61 \rightarrow 36.27$
θ_{23} [°]	48.6	$41.0 \rightarrow 51.5$
θ_{13} [°]	8.65	$8.26 \rightarrow 9.02$

Table 1.1: Table regrouping known values for neutrino oscillation parameters, assuming different neutrino mass orderings. NO = normal ordering; IO = inverted ordering. The parameter Δm^2_{31} is not listed in the table as $\Delta m^2_{31} = \Delta m^2_{32} + \Delta m^2_{21}$[1]

the following PMNS matrix

$$\mathcal{U} = \begin{pmatrix} 0.821 & 0.550 & 0.149 \\ -0.463 & 0.490 & 0.738 \\ 0.332 & -0.675 & 0.657 \end{pmatrix} \tag{1.32}$$

1.4.3 Neutrino mass ordering experiments

Experiments trying to determine the neutrino mass ordering are based on the fact that different NMOs generate a different neutrino oscillation pattern, hence different flavor-specific fluxes. The difference in observed fluxes with respect to each NMO can be measured in hope of assessing the actual NMO.

Several project aiming to discriminate the NMO based on the study and measurement of neutrino oscillations currently exist. A non-exhaustive list includes :

- NOνA (NuMI Off-axis electron neutrino Appearance): it is a long-baseline neutrino experiment which uses a beam of neutrinos produced at Fermilab in an accelerator. It focuses on the measure of the NMO-specific $\bar{\nu}_e/\nu_e$ appearances and $\bar{\nu}_\mu/\nu_\mu$ disappearances.[17]

- Super-Kamiokande: it is a water Cherenkov detector. Super-Kamiokande aims to, among other things, measure the neutrino mass hierarchy by observing atmospheric neutrinos and beam-neutrinos from a proton accelerator. For the atmospheric neutrinos observation, it aims to measure the matter effects on the oscillation probabilities [18].

- JUNO experiment: it is a liquid scintillator detector aiming to measure the neutrino mass hierarchy mainly by observing the oscillations of reactor $\bar{\nu}_e$ from two equidistant nearby nuclear power plants. It aims to observe the NMO-dependent interference in neutrino oscillations which is the phase difference in the vacuum neutrino oscillations [19].

This master thesis focuses on the NMO discrimination with the JUNO experiment, exploiting supernova neutrinos instead of reactor neutrino data.

In addition to determining the mass hierarchy and oscillation parameters, numerous experimental outcomes are being sought through neutrino observations to investigate physics beyond the Standard Model. Besides the NMO determination through reactor neutrinos, the next generation of neutrino experiments (including JUNO) search to solve open problems which include the assessment of wether or not neutrinos are Majorana particles and violate CP symmetry through the observation of a double-beta decay, neutrino signals as a measure of dark matter existence, measuring the hypothetical existence of sterile neutrinos [20–22] ...

Chapter 2

Core-collapse supernovae as neutrino messengers

This chapter begins with a brief description of a heavy star's evolution. After the stellar evolution, a discussion of its end of life follows along with a full but qualitative description of the core-collapse supernova phenomenon, in agreement with current state of the art knowledge. The core-collapse phenomenon is then viewed from the neutrino point of view and how it is of interest for neutrino observatories.

2.1 Stellar evolution

When the core of a massive protostar reaches a certain threshold temperature, a star is formed (considered here $M \geq 8\mathrm{M}_{\odot}$) and it enters the main sequence of its life. During the main sequence, the star maintains its internal pressure and temperature through nuclear fusion of hydrogen into helium in its core. As the core becomes hotter and denser, the fusion of heavier elements in the star is possible. When the core runs out of usable nuclear fuel, the core collapses. This core collapse triggers a rebound shock wave that expels the star's outer layers in a supernova explosion. The term "core-collapse supernova" (CCSN) refers to both the core collapse and the subsequent supernova explosion triggered by the rebound shock wave.

2.1.1 Main sequence

The stellar nucleosynthesis cycle starts when the core hits $\sim 10^7\,\mathrm{K}$ [23]. In this state one particular fusion becomes energetically possible, the fusion of hydrogen, which happens mainly through the proton-proton cycle or the CNO-cycle. Through both these cycles, the star converts hydrogen into helium and also releases heat as fusing elements with a lower binding energy per nucleon into heavier elements is an exothermic process [24]. The new helium atoms are heavier than the hydrogen atoms and pile up at the center of the star, thus creating a new core inside an outer layer of hydrogen, the light nuclei they come from.

As the fusion of hydrogen gradually stops, the outer layers compress the core as there is not enough outwards thermal pressure anymore coming from the fusion. The compression of the core increases its temperature and pressure until the fusion of the next element is possible, in this case helium. This periodic fusing of light elements into heavier and heavier elements goes on until the fusion of silicon, which eventually decays into iron-56. This is the last step of the stellar nucleosynthesis because the fusion of iron-56 is not exothermic anymore since iron-56 has the highest binding energy per nucleon of all elements.

At this point, the star has an inner core of iron-56 atoms, covered with several outer layers of elements of decreasing weight giving the structure illustrated in Fig. 2.1. Now that the star cannot create outwards pressure anymore through the thermal energy release from the core fusion, it cannot counteract the gravitational forces of the outer layers anymore. The star tends to its inevitable collapse as the outer layers gradually compress its core and eventually the electron degeneracy pressure cannot withstand the gravitational compression, the electron degeneracy pressure being the pressure created by condensed electrons which follow a Fermi-Dirac statistics and thus cannot occupy the same energy levels [25]. When the iron-core gets to the Chandrasekhar limit $M = 1.4\mathrm{M}_{\odot}$, the gravitational collapse takes place [23].

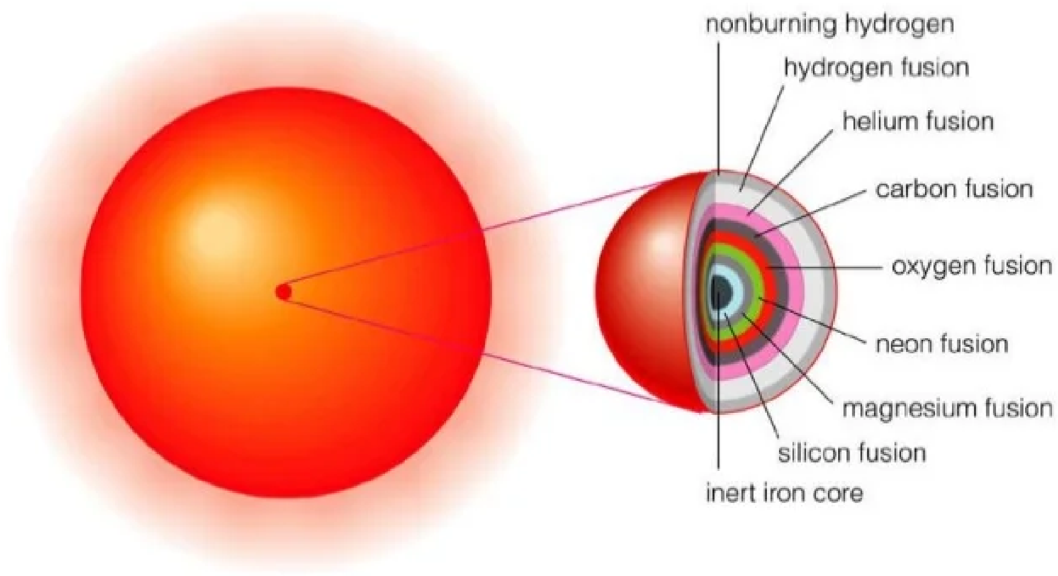

Figure 2.1: Stellar structure in the final stage of the main sequence [26]

2.1.2 Core collapse supernova : a neutrino-driven explosion

Once the Chandrasekhar limit is reached, the core collapses due the uncompensated gravitational pressure from the outer layers and the CCSN begins. The CCSN is however not an instantaneous phenomenon and, as currently believed, is composed of three basic phases, preceded by a phase of infalling matter, which are illustrated in detail Fig. 2.2; a phase of infalling matter on the core (panel 1-2), a bounce of this supersonic matter wave on the core when it cannot be anymore compressed (panel 3-4), a stalling of this wave after energy losses (panel 5) and finally a revive of the stalled wave resulting in the actual explosion (panel 6).

To start with, just before the actual core-collapse, the star's outer layers are contracting the core which has a density of around $\rho = 10^{10}$ g/cm^3. As the core gets compressed from the infalling matter of the outer layers, two major phenomena occur. One is the electron capture

$$p + e^- \rightarrow n + \nu_e \tag{2.1}$$

and the second is the photodisintegration of ^{56}Fe originating protons and neutrons in the chain. These two reactions result in a neutron-rich core, reducing the electron degeneracy pressure, and an overall pressure loss with respect to the infalling outer layers.

As the core now gets compressed to about $\rho = 10^{12}$ g/cm^3, the ν_e created through electron captures on infalling matter get trapped as their average diffusion time becomes larger than the collapse time [27]. The core then further gets contracted until the core density reaches the nuclear density $\rho = \rho_0 = 10^{14}$g/cm^3 at which point the core physically cannot be contracted anymore and a sudden stop is put to the infalling matter. This sudden stop creates an outwards shock wave, the core bounce. The core bounce travels through supersonic infalling matter, dissociating heavy nuclei on its way, losing energy and eventually stalling at a radius of 100-200 km.

When the core bounce reaches a density such that it becomes transparent to neutrinos, all the ν_e produced can finally escape the shock and get released in a big burst called the ν_e burst which lasts ~ 10 ms and starts a few ms after the core bounce.
Now that the core bounce shock wave is stalled, matter keeps falling inwards and piling up on the core, heating the outer layers of the forming proton neutron star (PNS). Neutrino-antineutrino pairs are created through thermal reactions in all flavors, everywhere in the collapsing core.

Neutrinos thus created leave the neutrino sphere and desposit their energy in the region between the neutrino sphere and the stalled shock wave. In this region, the gain layer, a net energy deposition takes place and pressure builds up. Eventually enough energy is deposited and enough pressure builds up to revive the shock wave, which results in the supernova explosion. With the supernova explosion, the mass accretion of the PNS is also put to a stop.

After the star exploded, the PNS cools down and still emits a neutrino signal which remains detectable on earth for ~ 10 s. If the initial star was massive enough, the PNS could at this point collapse into a black hole. The fact that massive CCSNe result in its massive remnant collapsing in black hole is an agreed upon idea but concrete evidence on the conditions in which that happens has yet to be found.

The outline of the sequence of events constituting a core-collapse supernova in this section are taken from the state of the art report made by the JUNO collaboration in order to prepare for CCSNe neutrino signal measurements [13] and H.A. Bethe's benchmark work in 1990 [27].

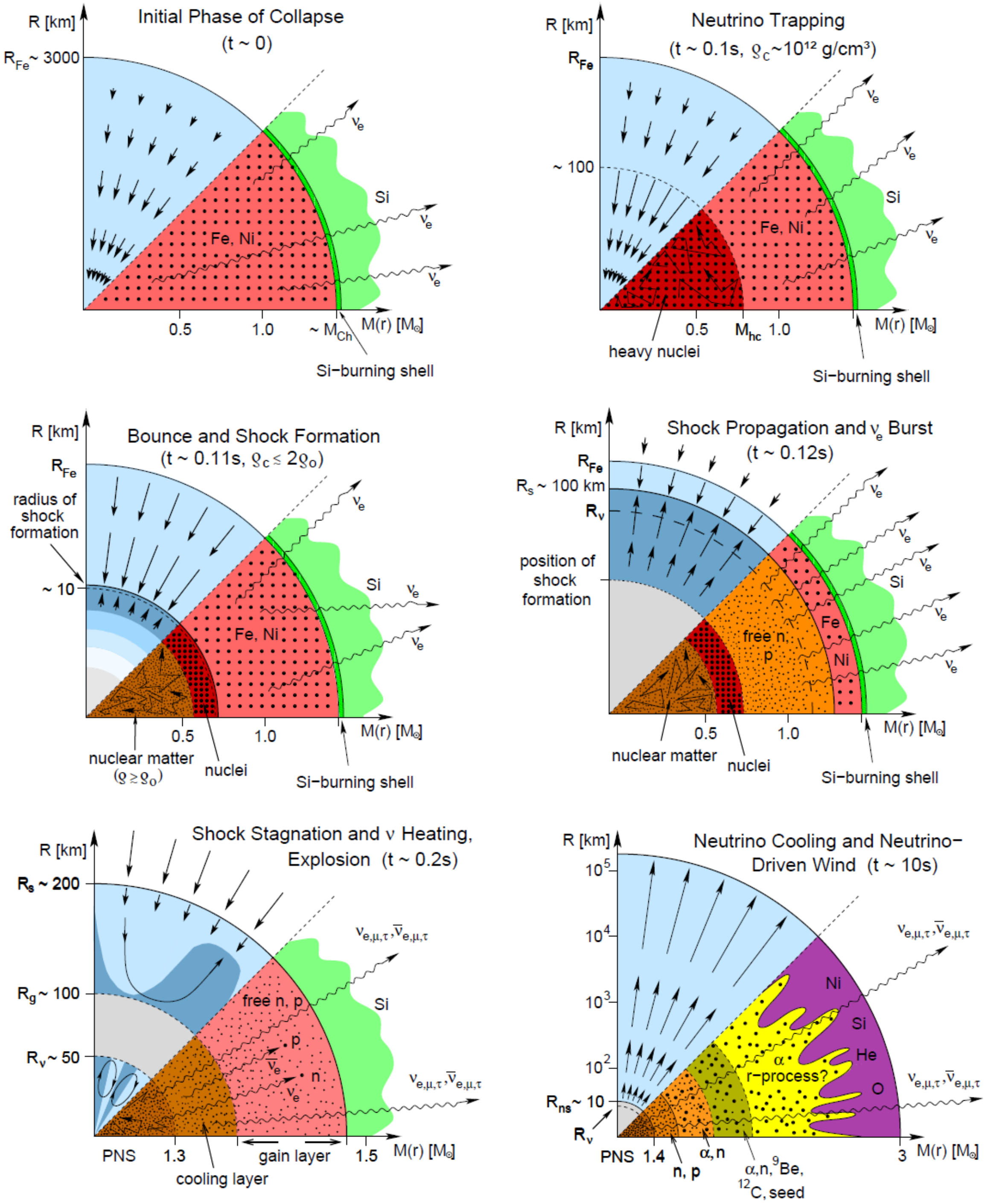

Figure 2.2: The different stages of a stellar core-collapse with eventual supernova explosion and cooling phase. The upper half of each quadrant shows the global mass movements while the lower half show the nuclear processes at play. The horizontal axis gives mass information (M_{Ch} = Chandrasekhar limit, M_{hc} = mass of collapsing inner core) while the vertical axis show the different radii R_i (Fe = iron core radius, s = shock radius, g = gain radius, ns = neutron star radius, ν = neutrinosphere) [28]

2.2 CCSN neutrino signal and experimental value

CCSNe are currently subject of a lot of research projects as they are not a fully understood phenomenon. However, if they happen according to the neutrino-driven explosion mechanism as described in the previous section, the CCSN can be divided into three neutrino-emitting phases that are of use for neutrino observation experiments: the neutrino burst, the accretion phase and the proton-neutron star cooling.

Here, as $\nu_{\mu/\tau}$-$\bar{\nu}_{\mu/\tau}$ pairs are created in basically equal amounts through thermal processes, they are designated by ν_x alltogether while for ν_e and $\bar{\nu}_e$ the dynamics remain different enough as to treat them separately [13].

1. **Neutrino burst :** During the core collapse, before the bounce, ν_e emission starts to rise as electron capture becomes energetically possible and favourable in the dense layers and core. Afterwards, the big compression from the bounce formation transiently reduces the neutrino emission signal for a few ms and, concomitantly, $\bar{\nu}_e$ emission starts to appear. After the ν_e burst is over ($\sim$ 10 ms after bounce), ν_x fluxes also start to rise as neutrino-pair productions become possible in the heated matter.

2. **Accretion phase :** After the neutrino burst and the bounce, matter piles up on the core for hundreds of ms. The neutrino signal is fed by the accretion flow in which ν_e are emitted through electron capture on infalling e^-. In the early stages of the accretion, the luminosity of ν_e-$\bar{\nu}_e$ is almost twice as intense than that of ν_x. After $\sim$ 200 ms, the explosino takes place and the luminosity drops, which corresponds to the infall of the outer Si-O layers.

3. **Cooling :** After the supernova explosion has passed the PNS maintains some neutrino radiation, equally for all flavors. The luminosity eventually drops after $\sim$ 10 s.

Each phase has thus its own signature, as can furthermore be seen on Fig. 2.3. Each of the phases will bring different information and allow to study different physics related to CCSN. As is explained more explicitely in the next section, this work focusses on the ν_e burst phase and its associated NMO-specific signatures that can be told apart in a neutrino observatory.

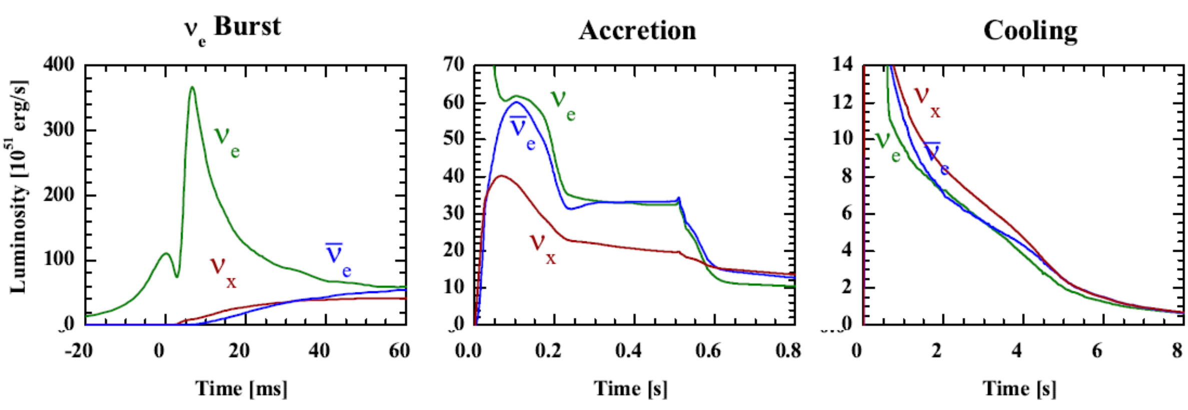

Figure 2.3: 27 $M_\odot$ CCSN simulated neutrino luminosity curves (green : ν_e, blue: $\bar{\nu}_e$, red : $\nu_x = \nu_{\mu,\tau}, \bar{\nu}_{\mu,\tau}$) for the three neutrino emission phases. This simulation from the Garching group uses a spherically symmetric model and a manually triggered explosion [13]

2.2.1 Experimental value of supernova neutrinos

When considering a core-collapse supernova, The neutrino fluxes F_{ν_i} reaching the Earth are function of the initially emitted neutrino fluxes $F^0_{\nu_i}$ and neutrino mixing physics through the survival probabilities $p/\bar{p}$. Their expressions can be written in all generality as follows

$$F_{\nu_e} = pF^0_{\nu_e} + (1-p)F^0_{\nu_x} \tag{2.2}$$
$$F_{\bar{\nu}_e} = \bar{p}F^0_{\bar{\nu}_e} + (1-\bar{p})F^0_{\nu_x} \tag{2.3}$$
$$4F_{\nu_x} = (1-p)F^0_{\nu_e} + (1-\bar{p})F^0_{\bar{\nu}_e} + (2+p+\bar{p})F^0_{\nu_x} \tag{2.4}$$

where $p/\bar{p}$ is the survival probability of a neutrino/antineutrino after propagating through the CCSN matter and space and neglecting matter effects for those neutrinos crossing the Earth, which are indeed irrelevant for the CCSN neutrino energies. Here, the $\nu_{\mu,\tau}/\bar{\nu}_{\mu,\tau}$ ($=\nu_x$) are all treated equally because their interactions when moving through the CCSN matter are very similar and it makes the formalism easier to work with [29].

Now to compute the NMO-dependent flux $F^{\mathrm{NMO}}_{\nu_i}$, one needs to take into account the different resonances that neutrinos can undergo, modifying these probabilities and resulting in a flavor change [30].

Assuming the standard case of the adiabatic MSW effect [31], for the NO case, the resonances create an almost complete exchange between the ν_x and ν_e spectra and for the IO case, on the contrary, the resonance happens at a different stage, and affects the anti-neutrinos [29]. As a result of these resonances, assuming only ν_e are created during the neutrino burst phase and neglecting the terms of order $\sin^2\theta_{13} \sim 10^{-5}$, one finds the survival probabilities as listed in Table 2.1 and the expressions (2.5-2.8) for the neutrino flux arriving on Earth [29].

$$F^{\mathrm{NO}}_{\nu_e} = p^{\mathrm{NO}}F^0_{\nu_e} + (1-p^{\mathrm{NO}})F^0_{\nu_x} \approx 0 \tag{2.5}$$
$$2F^{\mathrm{NO}}_{\nu_x} = (1-p^{\mathrm{NO}})F^0_{\nu_e} + (1+p^{\mathrm{NO}})F^0_{\nu_x} \approx F^0_{\nu_e} \tag{2.6}$$

$$F^{\mathrm{IO}}_{\nu_e} = p^{\mathrm{IO}}F^0_{\nu_e} + (1-p^{\mathrm{IO}})F^0_{\nu_x} \approx \sin^2\theta_{12}F^0_{\nu_e} \tag{2.7}$$
$$2F^{\mathrm{IO}}_{\nu_x} = (1-p^{\mathrm{IO}})F^0_{\nu_e} + (1+p^{\mathrm{IO}})F^0_{\nu_x} \approx \cos^2\theta_{12}F^0_{\nu_e} \tag{2.8}$$

A detector which is able to detect ν_e would thus measure, around the ν_e burst phase of the CCSN, an intense peak in the IO case, but an absence of such peak in the NO case. This is the NMO sensitivity this master thesis will focus on.

After the ν_e burst however, the emission of the other neutrino flavors starts to get important and this NMO sensitivity falls off.

Neutrino mass ordering	p	$\bar{p}$
NO	~ 0	$\cos^2\theta_{12}$
IO	$\sin^2\theta_{12}$	~ 0

Table 2.1: Survival probabilities $p/\bar{p}$ for CCSN neutrinos/antineutrinos for the two NMOs

Chapter 3

The Jiangmen Underground Neutrino Observatory

The JUNO experiment is presented in this chapter, discussing its scope, structure and detection characteristics. After, the tools set up at the JUNO experiment to identify the neutrino mass ordering using supernova neutrino signals are presented.

3.1 The JUNO experiment : an overview

The Jiangmen Underground Neutrino Observatory (JUNO) experiment is a medium-baseline multi-purpose neutrino experiment, buried ~ 700 m underground, whose main purpose is the assessment of the neutrino mass ordering through the observation of reactor antineutrinos. It has been shown that after six years of data taking, JUNO will be able to determine the NMO at a $3-4\,\sigma$ confidence level [19].

JUNO's unprecedented energy resolution, number of discernable events and baseline optimization (cf. Fig. 1.3) will furthermore allow precise measurements of the neutrino oscillation parameters as well as assessing other neutrino-related open questions [4]. It has also been shown that after six years of running, JUNO will be able to determine the neutrino oscillation parameters with a sub-percent precision [19]

The JUNO experiment is located in Jinji town in the Guangdong province (Fig. 3.1), at 53 km of two nuclear powerplants (NPP), the Yangjiang and Taishan powerplants. This location has been chosen based on the fact that the baseline that gives the best NMO discrimination power when observing reactor antineutrinos is around 53 km [4].

3.1.1 The JUNO detector

The JUNO detector has two main components : the veto detector, composed by the muon top tracker (TT) and the water Cherenkov detector (WCD), and the central detector (CD) as schematically shown in Fig. 3.4.

The WCD is a cylindrical pool with a diameter of 43.5 m and a height of 44 m, filled with 35 kton of ultrapure water. The extreme purity of water is necessary to

Figure 3.1: Location of the JUNO experiment at 53 km of Yangjiang NPP and Taishan NPP, the JUNO-TAO facility at Taishan serves as reference observatory of the $\bar{\nu}_e$ fluxes [19]

avoid background noise in the form of impurity disintegrations. The light (Cherenkov photons/radiation) produced by muons is reflected on the inner core of the cylinder, which is covered in reflective foils, and/or detected with the 2400 20-inch photomultiplier tubes (PMT) placed on the outer shell structure of the CD.

The TT is a plastic scintillator system that is used to track incoming muons. It is composed of several 6.7 m^2 square TT walls placed side by side, with a 15 cm overlap, on three layers with each TT wall composed of 512 scintillator strips that will detect the muons, tracking their path (Fig. 3.2) [32].

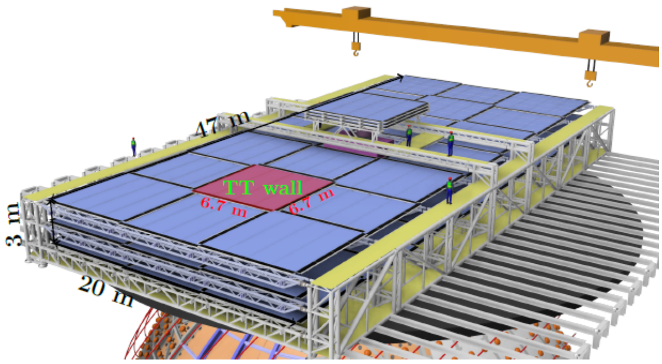

Figure 3.2: JUNO experiment Top Tracker [19]

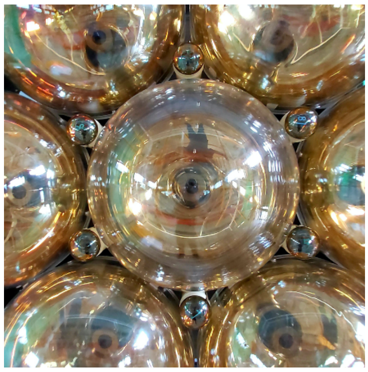

Figure 3.3: JUNO CD large PMT and small PMT system [19]

Together, they thus form a double muon veto system or the veto detector. Indeed, muons are a threat to $\bar{\nu}_e$ observations as they generate ^{9}Li and ^{8}He, which are β-emitting and n-emitting isotopes, and fast neutrons which can imitate the IBD signature for which the CD is tuned. It is thus important to have this muon veto system to distinguish between muon-induced reactions and radioactivity in general from $\bar{\nu}_e$-IBDs. The TT is expected to be very effective for atmospheric muons as $\frac{1}{3}$ of all atmospheric muons entering the CD will cross the TT, where their path will be tracked and extrapolated into the CD giving a very efficient veto mechanism. For other muon sources, the veto system relies on the WCD and CD only [19].

The CD is an acrylic sphere, with an inner diameter of 35.4 m. It will be filled with 20 kton of organic liquid scintillator (LS), making up around 1.5×10^{33} target protons [13]. The LS requires a high level of purity, which is achieved by a dedicated purification system, and is composed of three compounds : Linear Alkyl Benzene (LAB), 2,5-diphenyloxazole (PPO), and 1,4-bis(2-methylstyryl)benzene (bis-MSB) which have a high light yield and show adequate transparency [19].

The inside of the acrylic sphere is coated with 17 612 "large" 20-inch PMTs to capture the scintillation signals and 25 600 "small" 3-inch PMTs filling the gaps the large PMTs leave when evenly distributed (Fig. 3.3). The small PMTs' purpose is manifold; as they accumulate events over time (in a narrower energy window than the large PMTs) they can serve as a reference for the detector overall reducing thereby some uncertainties and improving the energy resolution and absolute uncertainty. They will also extend the dynamic range of the detector and, with their good time resolution, they will help the event reconstructions [19].

The relative energy resolution required for the determination of the NMO with reactor $\bar{\nu}_e$ at the desired confidence level is $\frac{\sigma}{E} = \frac{3\%}{\sqrt{E}}$ where $E = 1\,\mathrm{MeV}$ is the visible energy in the detector [13], this resolution is expected to be achieved by JUNO, as reported in [33].

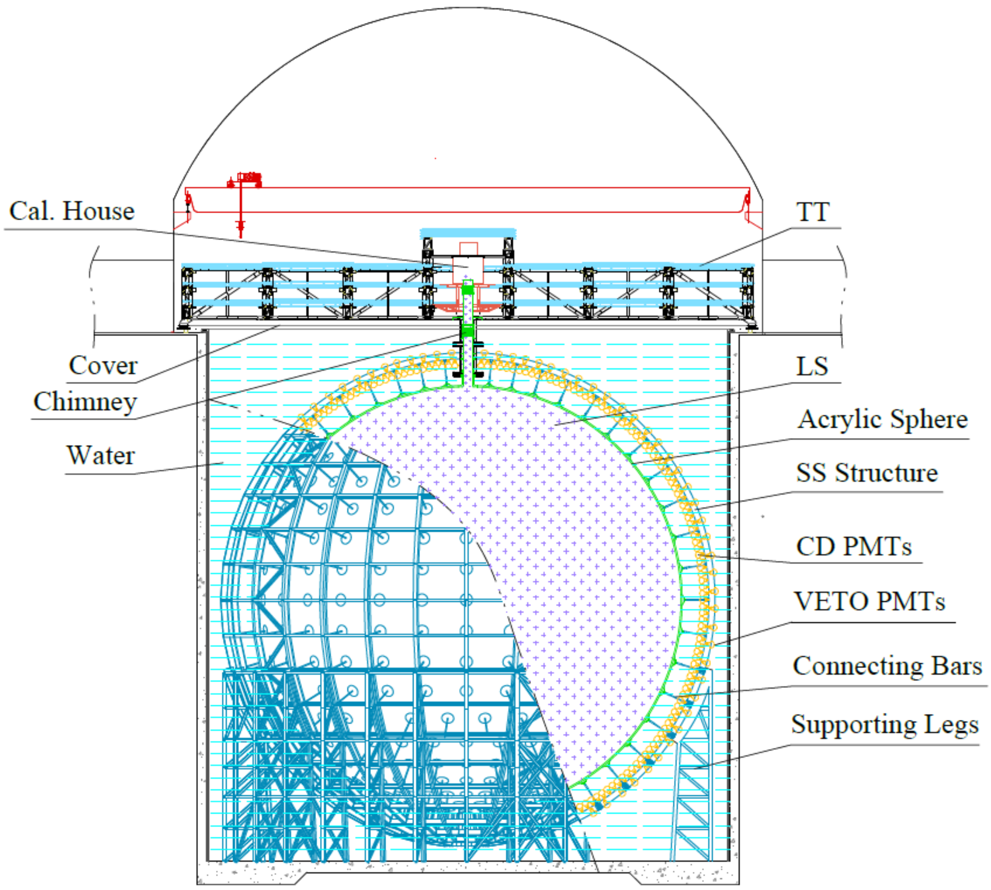

Figure 3.4: The JUNO detector [19]

3.1.2 Measurements with JUNO

The main purpose of JUNO is to assess the NMO through the observation of reactor antineutrinos. JUNO observes the reactor antineutrinos through the CC inverse beta decay reaction (IBD) in the CD

$$\bar{\nu}_e + p \rightarrow e^+ + n \tag{3.1}$$

The reactor $\bar{\nu}_e$ interact with the LS protons, creating a positron and a neutron; the positron almost immediately deposits his surplus energy T_{e^+} and annihilates with a surrounding e^- generating 2 γ rays at 180° of total energy $E = 2 \cdot 511\,\mathrm{keV}$, while the neutron takes a while to thermalize, ($\sim$ 200 µs) and eventually releases a 2.2 MeV γ after it is captured (5.4 MeV if the capture happens on carbon nuclei).

The neutrino energy can be inferred by reconstructing the positron energy and using the kinematics (energy threshold) of the reaction $E_\nu^{\mathrm{th}} = m_e + m_n - m_p \approx 1.804\,\mathrm{MeV}$, and thus $E_\nu = 1.8\,\mathrm{MeV} + T_{e^+}$. Furthemore, the IBD has an easily identifiable signature, both in time (prompt and delayed γ signals) and energy ($E_{\gamma_{\mathrm{delayed}}} = 2.2$ MeV) making it a handy reaction [4].

In order to identify the NMO with reactor antineutrinos, JUNO utilizes the survival probability of electron neutrinos, Eq. 1.30, in its unsimplified version

$$P_{\bar{\nu}_e \rightarrow \bar{\nu}_e} = 1 - \sin^2 2\theta_{13} \left(\cos^2 \theta_{12} \sin^2 \Delta m_{31}^2 + \sin^2 \theta_{12} \sin^2 \Delta m_{32}^2 \right) - \cos^4 \theta_{13} \sin^2 2\theta_{12} \sin^2 \Delta m_{21}^2 \tag{3.2}$$

In fact, the this survival probability shows an NMO-specific spectrum in the $\frac{L}{E}$-space. The reactor $\bar{\nu}_e$ energy spectrum thus contains a discernible difference, one NMO to the other, when considering a fixed and optimized L of around 53 km [19] The IBD reaction can at that point be used as a probe to measure the $\bar{\nu}_e$ flux and spectrum. The excellent energy resolution and high statiscs (in $\sim$ 6 years of data taking), will allow JUNO to determine the NMO with reactor $\bar{\nu}_e$.

JUNO is sensitive to a lot of neutrino sources however, through mainly but not only the IBD reaction; the neutrino sources JUNO is sensitive to are summarized Table 3.1.

Research	Expected signal	Energy region	Backgrounds
Reactor antineutrino	60 IBDs/day	$0 - 12$ MeV	Radioactivity, μ
Supernova burst 10kpc	5000 IBDs, 2300 ES	$0 - 80$ MeV	Negligible
DSNB (w/o PSD)	$2 - 4$ IBDs/year	$10 - 40$ MeV	Atmospheric ν
Solar neutrino	$\sim$ 100 eES per year for ^{8}B	$0 - 16$ MeV	Radioactivity
Atmospheric neutrino	$\sim$ 100 per year	$0.1 - 100$ GeV	Negligible
Geoneutrino	$\sim$ 400 per year	$0 - 3$ MeV	Reactor ν

Table 3.1: Detectable neutrino event sources in JUNO with event rate, energy window and associated background noise (ES: elastic scattering, eES: electron elastic scattering, DSNB : diffuse supernova neutrino background ; PSD : pulse shape discrimination). Figure adapted from [19].

This work focuses on the measurements that can be made with supernova neutrinos, following a CCSN at an observable distance, and how they can be of use for the NMO discrimination. As Table 3.1 illustrates, a CCSN brings a lot of events in the detector making it an information-rich event that cannot be missed.

The physical properties of a supernova neutrino flux and how they can be utilized in JUNO are discussed in the next section.

3.2 NMO determination with JUNO: application to supernova neutrinos

For a supernova at 10 kpc, around 5000 IBD and 2300 elastic scattering events are expected in JUNO. This exceptionally high statistics could allow to probe a lot of neutrino and supernova parameters.

In JUNO, CCSN neutrinos can be observed through different kinds of interactions. The main interaction channels and the corresponding number of expected events for different average neutrino energies are summarized in Table 3.2. The expected energy spectrum for a 10 kpc CCSN considering all the interaction channels listed in the table below is represented in Fig. 3.6.

Channel	Reaction	Type	Events for different $\langle E_\nu \rangle$ values		
			12MeV	14MeV	16MeV
IBD	$\bar{\nu}_e + p \rightarrow e^+ + n$	CC	4.3×10^3	5.0×10^3	5.7×10^3
Proton-neutrino ES	$\nu + p \rightarrow \nu + p$	NC	6.0×10^2	1.2×10^3	2.0×10^3
Electron-neutrino ES	$\nu + e \rightarrow \nu + e$	CC&NC	3.6×10^2	3.6×10^2	3.6×10^2
^{12}C	$\nu + {}^{12}\mathrm{C} \rightarrow \nu + {}^{12}\mathrm{C}^*$	NC	1.7×10^2	3.2×10^2	5.2×10^2
CC ^{12}C	$\nu_e + {}^{12}\mathrm{C} \rightarrow e^- + {}^{12}\ \mathrm{N}$	CC	4.7×10^1	9.4×10^1	1.6×10^2
CC ^{12}C	$\bar{\nu}_e + {}^{12}\mathrm{C} \rightarrow e^+ + {}^{12}\ \mathrm{B}$	CC	6.0×10^1	1.1×10^2	1.6×10^2

Table 3.2: Neutrino interaction channels in JUNO for a 10 kpc CCSN, adapted from [13]

This master thesis focuses on the three main interaction channels for CCSN neutrino signals in JUNO: the IBD channel, the neutrino-electron elastic scattering interaction (eES) and the neutrino-proton elastic scattering interaction (pES).

Electron elastic scattering

In order to be able to record information about ν_x, it is necessary for JUNO to be sensitive to NC interactions, since ν_x only interacts through NC reactions. In that sense, and despite its small cross-section, the eES interaction channel is an adequate probe for ν_x, as it is sensitive to all neutrino flavors [34].

However, for ν_e, the electron elastic scattering can proceed through both NC or CC channels, as is illustrad in the Feynman diagrams in Fig. 3.5, which slightly changes the interaction cross section for ν_e. This makes the detector sensitive to the ν_x/ν_e fraction of the CCSN neutrino flux.

The energy of the neutrino is reconstructed via the visible recoil energy spectrum from the scattered electron [36].

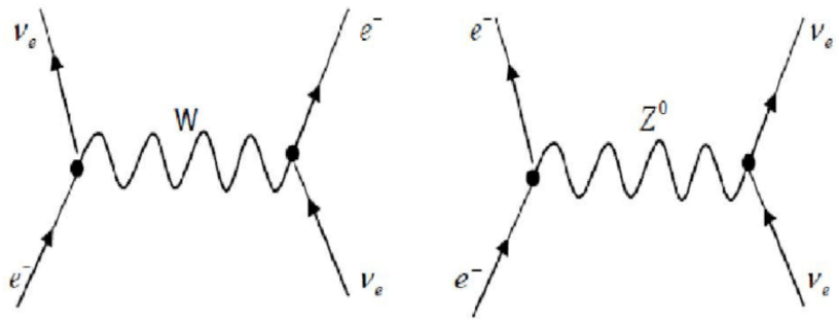

Figure 3.5: Feynman diagram of the CC $\nu_e - e^-$ interaction (left) and NC $\nu_e - e^-$ interaction (right) from [35]

Proton elastic scattering

The proton elastic scattering channel is a purely NC channel and is thus sensitive to all neutrino flavors as confirms the cross section expression [37]. Its cross section is much bigger compared to the eES cross section, resulting in ~ 2000 pES events against ~ 300 eES event for a 10 kpc CCSN (Table. 3.2). On the other side its cross section is about the same than the IBD cross section for $\bar{\nu}_e$ but at way smaller energies, furthermore its sensitivity to all neutrino/antineutrino flavors compensates [13].

The pES channel is thus an important interaction channel when observing three-flavoured neutrino fluxes like the CCSN neutrino flux, even though the three flavors are blended together.

Just like for electron elastic scattering events, the proton elastic scattering channel reconstructs the neutrino energy on the basis of the proton recoil kinetic energy [37].

Inverse beta decay

The inverse beta decay is the main interaction for CCSN neutrino signal, as for the reactor antineutrino flux, and follows the exact same physics and detection procedure as has been previously described.

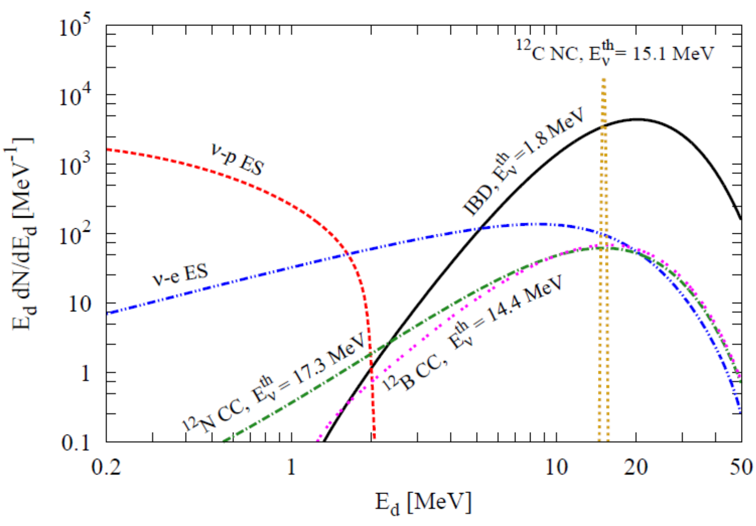

Figure 3.6: Neutrino event spectrum with respect to the visible energy E_d in JUNO for a 10 kpc CCSN, assuming no flavor conversions [13].

Chapter 4

Core-collapse supernova neutrino simulations for JUNO

This chapter first discusses two popular numerical models, and two neutron star equations of state, that are commonly used in the literature to simulate CCSNe. Then, some JUNO detection physics and its limitations are introduced to adapt the CCSN simulations to the detector. Finally, combining those models with the JUNO neutrino detection physics, the lightcurves measured in JUNO and how they are impacted by the different simulation parameters are discussed.

4.1 Supernova numerical models

Core-collapse supernovae, on all conceptual levels, are still not completely understood. They are very complex phenomena on one side and don't happen very often at an observable distance via neutrinos, making it difficult to acquire data to test the different theories, on the other side. Since the last observed CCSN in the Large Magellanic Cloud in 1987, the SN 1987A [38], a lot of effort has been put into developing theoretical models that would serve as a basis for numerical simulations. One of the fundamental component of such theoretical models is the set of equations of state (EoS) they are based upon. In all generality, an EoS is a theoretical description of hot and dense nuclear matter which when applied to a star's core as a whole " determines the structure of compact objects and their dynamics through its behavior of thermodynamic quantities" (K. Sumiyoshi, 2021). The particular combination of EoS describing the core's dynamics eventually leads to particular explosion mechanisms and content [39].

The EoS that are of interest in this work are the Shen EoS [40] and the Lattimer-Swesty (LS) EoS [41], which both get their name from the people who introduced them. The LS EoS set was the first CCSN EoS set to be introduced, it is based on the compressible liquid-drop model for nuclei and doesn't have any relativistic considerations. The Shen EoS on the other side is constructed using the relativistic mean-field (RMF) theory with the Thomas-Fermi approximation; the RMF theory considers relativistic effects by describing the nuclei as interacting Dirac nucleons [42] and the Thomas-Fermi approximation proposes a description of poly-electronic systems by modelling them as a degenerate Fermi-Dirac gas [43].

This work makes use of the CCSN numerical model developed by the Garching group [44] . The Garching 1D model, as used in this work, can use both the Shen EoS and the LS EoS.

4.2 Supernova detection characteristics for JUNO

In addition to the theoretical supernova modelling, this work involves the equally important simulation of the JUNO detector. The JUNO collaboration has developed a software environment that simulates all aspects of the JUNO detector's response [45]. This offline data processing software is based on the Geant4 toolkit [46], a simulation package computing particle-matter interactions, and built according to the SNiPER (Software for Non-collider Physics ExpeRiments) architecture, a unifying software framework that provides a common working environment for high-energy physics experiment [47].

The JUNO offline software, in line with the SNiPER framework, is divided into small components that together are able to simulate the complete chain of events of a CCSN (detection). Its 5-block structure is illustrated in Fig. 4.1 and is justified as follows [48]:

1. **Physics generator:** this block generates a neutrino flux, here a CCSN neutrino flux. It is in this particular case a vast numerical model, such as the one developed by the Garching group, which considers the star's EoS, the physics of the core collapse and the neutrino propagation. Then it convolves the neutrino flux with the detector geometry (number of targets) and interaction cross-sections (detector material). A Monte-Carlo based approach takes into account the detector geometry, LS composition and LS response.

2. **Detector simulation:** this block models the photon signal generation after the neutrino interaction, its propagation, absorption and the photomultiplier tube light response.

3. **Electronics simulation:** this part of the simulation software uses a Monte Carlo approach to simulate the electronics component to simulate the response of the PMTs and the following electronics readout system. This includes the electronics event trigger, as well as the PMT properties such as the transit time of photons. It also enables the study of signal processing, noise effects (dark noise, afterpulse), and the overall performance of the detector's electronic systems.

4. **Calibration :** The calibration of the JUNO detector is simulated according to its calibration system. It takes into account the physical and instrumental non-linearity of the detector, systematic uncertainties, etc [49]. This block is not explicitly shown on Fig. 4.1.

5. **Reconstruction :** The multiple reconstruction methods and blocks simulate the process of correlating the PMT pulses to the physical characteristics of the particle (energy, waveform, vertex (place of interaction)).

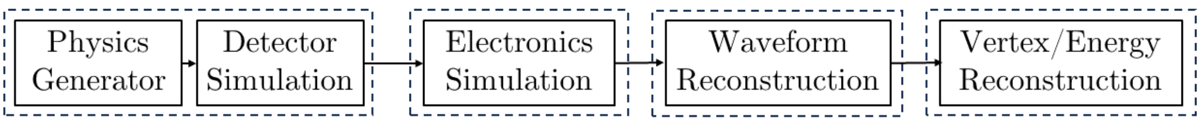

Figure 4.1: JUNO offline software's SNiPER-based structure, adapted from [50]

A perfect detection efficiency is considered at the detector simulation level, but a 0.1 MeV energy cut-off is applied on measured events as below 0.1 MeV JUNO cannot make the distinction between background noise and such a low energy physics/neutrino event. The JUNO project was initially designed with a 0.2 MeV trigger [51], but recent developments lead to believe 0.1 MeV will be possible [52].

This work does not consider the simulation blocks beyond the detector simulation phase. Conclusions are drawn based solely on the CCSN and JUNO detector physics, the electronics simulation and reconstruction blocks are disregarded. To sum up, this study focuses on the CCSN neutrino flux generator, the interaction of neutrinos with JUNO and the methods used to extract information on the NMO from them.

4.3 Supernova neutrino lightcurves: parametric-wise analysis

The goal of this section is to present the main observable of interest when treating with CCSN data: the time profile or lightcurve. The lightcurves will be compared for different models and physics (i.e. EoS or NMO hypotheses). In this work, lightcurves are defined as the time spectra of visible events in JUNO, they are curves containing the instants t of every measured event. Lightcurves differ from luminosity curves (briefly shown in Fig. 2.3) as they do not contain energy information, but rather count measured events in the detector and possibly identify their nature (eES, pES, IBD). They represent what JUNO will, among other things, concretely be able to detect. This signal analysis of CCSNe is not completely straightforward and several parameters need to be taken into account.

On one side, it is not known what mass the progenitor will be or at what distance the next CCSN will occur, besides already the big uncertainty on when the next CCSN will happen [53]. And on the other side, it is not known how CCSNe exactly occur and thus several models describing the underlying physics have been developed to simulate the explosion.

In the hope of understanding how JUNO would be able to determine the NMO based on CCSN neutrino signals, the impact of these simulation parameters need to be individually assessed and discussed.

4.3.1 Impact of the progenitor mass

Complete CCSN numerical models however do use the progenitor mass as a parameter as it is an important initial condition.

Physically, the progenitor mass together with the radius and metallicity (i.e. the compactness) is the most relevant parameter regarding the initial conditions of the collapsing stellar core. Higher-mass progenitors have larger cores, which undergo more extensive gravitational collapse due to their larger gravitational binding energy. During the core collapse, the strength and energy of the shock wave are influenced by the progenitor mass as higher-mass progenitors tend to produce more energetic shock waves. Finally, as 99% of the explosion energy is emitted in the form of neutrinos, the progenitor mass affects the neutrino emission characteristics, with higher-mass progenitors thus producing more intense neutrino fluxes.

When comparing the lightcurves for different progenitor masses, the previously hypothesized influence is clear: heavier progenitors do generate more energetic supernova explosions. The difference in the number of expected events starts to rise after the bounce which can be seen in both plots of Fig. 4.2.

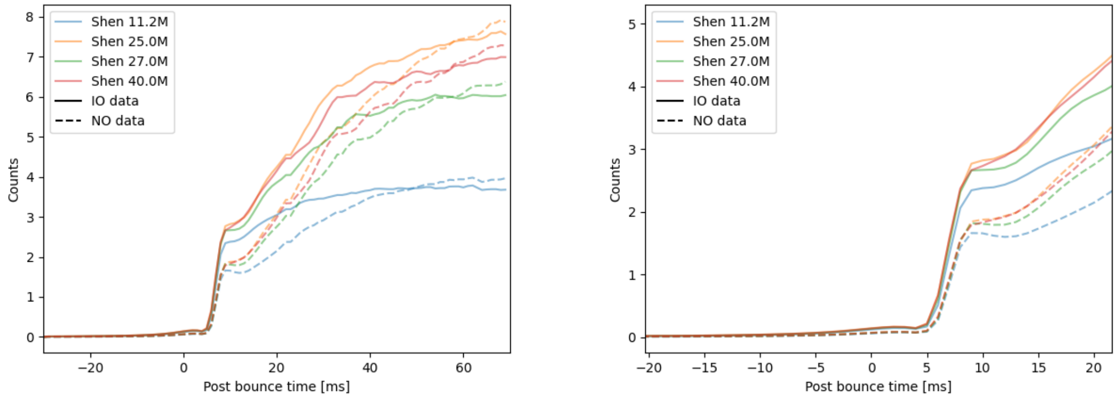

(a) Full ν_e burst phase

(b) Zoomed around the bounce

Figure 4.2: Lightcurves for supernova bursts of different progenitor masses, for the Shen EoS used by the Garching group numerical model. The CCSNe are taken to be at a 10 kpc distance. Solid lines represent the case of inverse neutrino mass ordering and the dashed lines the normal ordering case.

4.3.2 Impact of the distance

The number of events detected in a neutrino observatory like JUNO after a supernova burst is a function of the CCSN distance through an inverse square law [54].

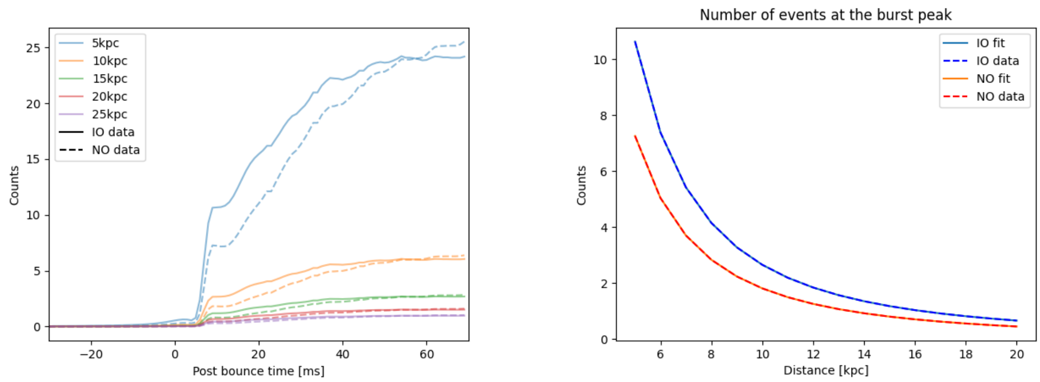

(a) Lightcurves for different CCSN distances

(b) Number of events at the ν_e burst peak in function of the SN distance with a $\frac{1}{d^2}$ fit

Figure 4.3: Influence of the distance of the CCSN on the lightcurve and the number of events detected in JUNO. The simulated CCSNe are of 27 $M_{\odot}$ and use the Garching group LS EoS numerical model.

As expected, the data matches the $\frac{1}{d^2}$ fit on Fig. 4.3b, the distance of the SN explosion has no influence on the shape of the measured lightcurves and simply applies a scaling factor to the number of events. Hence, for the sake of the NMO discrimination, it would be advantageous to observe a relatively nearby supernova burst in order to have more signal statistics. The $\sim$ 7300 events predicted (Fig. 3.1) over the whole supernova burst at 10 kpc would double to about 29200 for a supernova at 5 kpc, which is not negligible at all.

4.3.3 Impact of the equations of state

Given the different EoS simulated in Fig. 4.4, the equations of state do not seem to have an impact on the early stages of the supernova explosion and around the ν_e burst peak. However after about $\sim$ 20 ms and independently from the progenitor mass, the lightcurves of each EoS start to diverge and show signs of model/EoS dependency.

The difference generally emerging after 20 ms, or more generally becoming significant at 20 ms, is consistent with the literature and stems from the fact that the ν_e burst is a relatively well understood phase of the supernova, the behaviour of which is independent from the used EoS or even the progenitor mass [36]. After the ν_e burst peak the lightcurves follow each a different dynamic, proper to the EoS used. The Shen EoS produces a larger number of events compared to the Shen EoS.

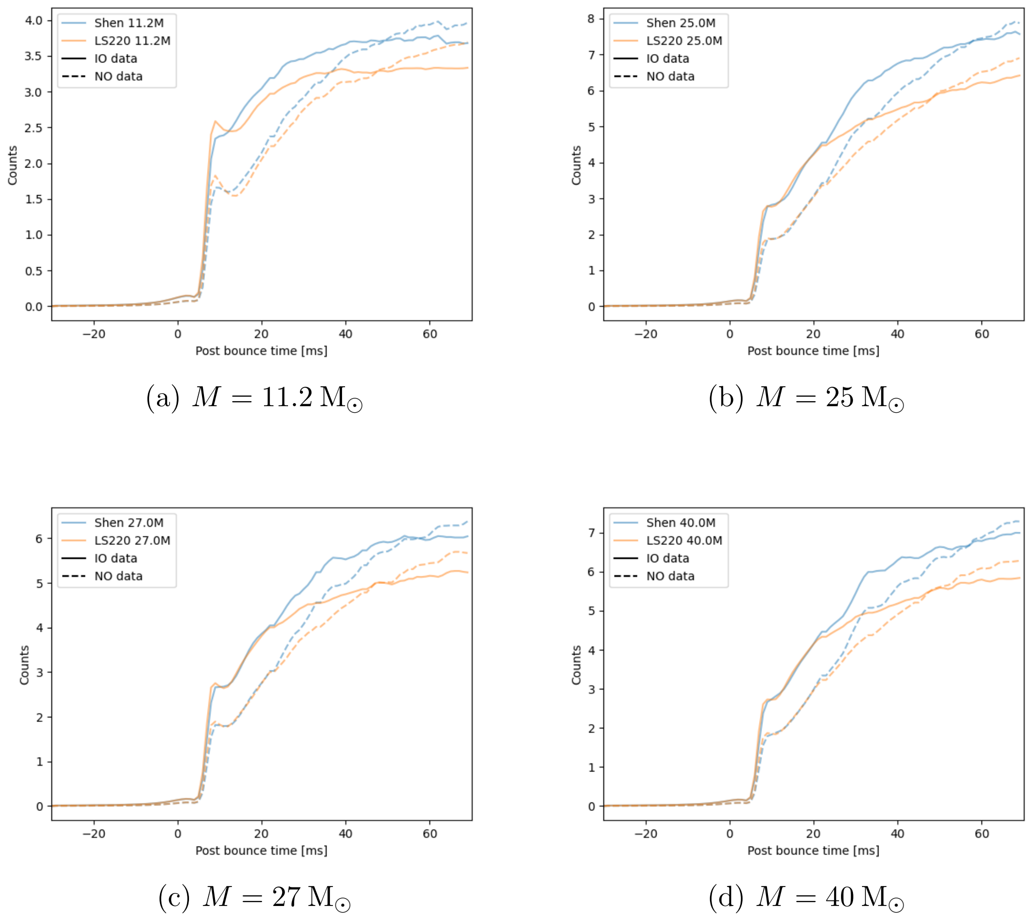

(a) $M = 11.2\,\mathrm{M}_\odot$

(b) $M = 25\,\mathrm{M}_\odot$

(c) $M = 27\,\mathrm{M}_\odot$

(d) $M = 40\,\mathrm{M}_\odot$

Figure 4.4: Lightcurves for different progenitor masses comparing the Shen EoS and the LS EoS using the Garching group numerical model. The CCSNe are at 10 kpc.

4.3.4 Comparison of the interaction channels

The different stages of the supernova explosion are characterized by time-varying flavor emissions and neutrino energy spectra. It is thus useful, in the broader aim of later assessing the NMO, to separate the different interaction channels and assess their respective lightcurves.

Proton elastic scattering

The proton elastic scattering (pES) is a NC interaction and it is, as has been described before, a color-blind interaction channel. When observing CCSNe, NC reactions are therefore of considerable importance as they allow to perform $\nu_x/\bar{\nu}_x$ measurements.

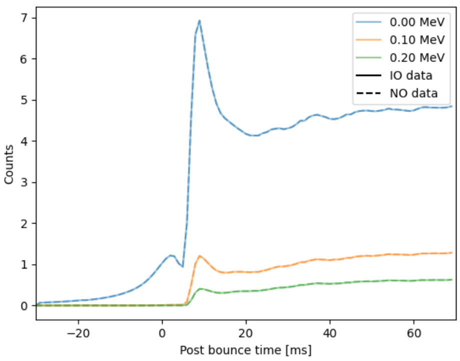

(a) Lightcurves for different energy thresholds

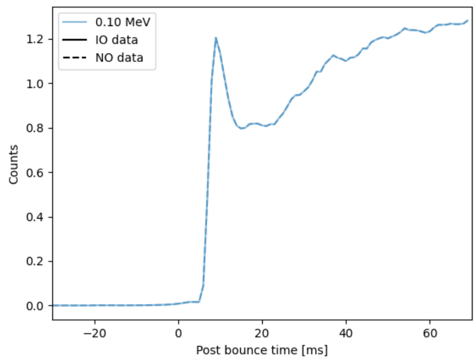

(b) Lightcurve for for JUNO global trigger energy threshold

Figure 4.5: Lightcurves for the pES interaction channel showing the strong influence of the energy-cut off on the time spectrum. The Garching group numerical model with the Shen equation is used for this plot, simulating a 27 $M_\odot$ at 10 kpc CCSN.

The proton elastic scattering channel is however very sensitive to the energy detection threshold of the experiment. There is more than a factor 10 difference between the number of events at the peak when no energy threshold is applied or only events above 0.2 MeV are kept, as can be seen on Fig. 4.5a. The big discrepancy between these two situations can be explained by looking at the event spectrum in JUNO for a 10 kpc CCSN (Fig. 3.6). At 0.20 MeV, the lower limit of the graph, $\sim 10^3$ events are expected for the pES channel. By slightly extrapolating the event spectrum, it becomes apparent that a lot events are being discarded when applying an energy cut-off of 0.00, 0.10 or 0.20 MeV.

The extra statistical power coming from perfectly detecting all events regardless of background noise would be very useful but it is not realistic, which is why the energy threshold of 0.1 MeV achieved by the JUNO global trigger is used (see Fig. 4.5b).

Finally, concerning the NMO, the pES channel shows strictly zero NMO sensitivity on its own. This is consistent with the fact that the NC p-ν scattering reaction is not dependent on flavor transformations but only on number of neutrinos and the fact that the NMO only impacts the flavor mix of a supernova explosion but not the total number of evetns. This is valid for all masses and EoS as illustrated in Fig. 4.6.

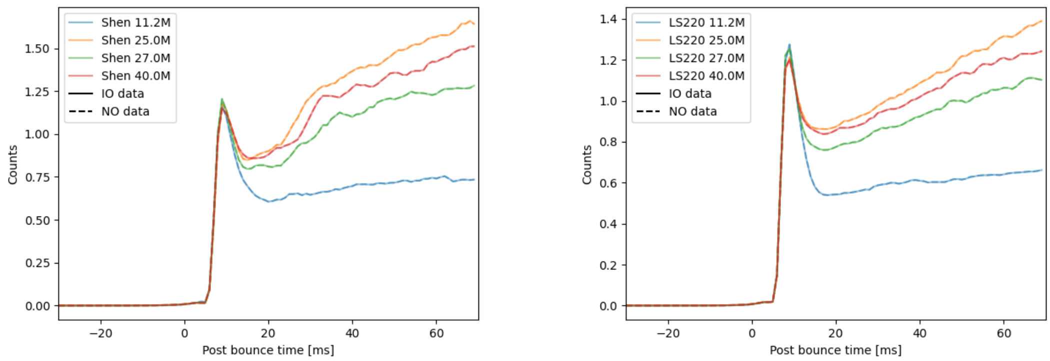

(a) Shen EoS

(b) LS EoS

Figure 4.6: Lightcurves for the pES interaction channel, considering the 0.10 MeV energy cut-off, for both EoS using the Garching group numerical model and for different progenitor masses. The CCSN is taken to be at 10 kpc.

Electron elastic scattering

The electron elastic scattering (eES) interaction channel is a neutral current interaction as well, making it sensitive to all neutrino flavors. Things are changing however compared to the pES channel as for the ν_e, the eES reaction can happen through NC or CC interaction channel when the lepton flavors are identical [34]. This brings some NMO sensitivity as the $\nu_e/\bar{\nu}_e$ fraction changes between the NMOs. The slight NMO sensitivity can be seen in Fig. 4.7a where the neutrino burst peak disappears in the NO case.

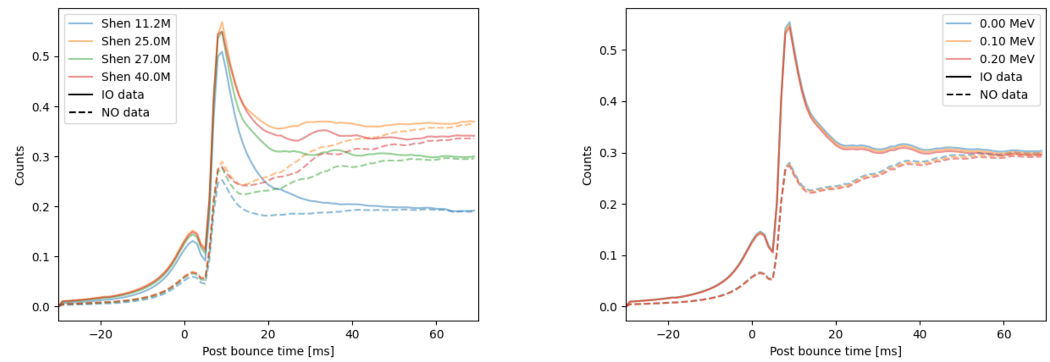

(a) Shen EoS

(b) Different cut-off energies with Shen EoS, 10 kpc, 27 $M_\odot$ CCSN

Figure 4.7: Lightcurves for the eES interaction channel for both EoS using the Garching group numerical model and for different progenitor masses. The CCSN is taken to be at 10 kpc.

The eES cross section is way smaller than the pES cross section, making it a weak interaction channel on its own [36].

The eES channel does not suffer very much from having different energy detection thresholds as can be seen in Fig. 4.7b. The slight - almost non-existent - discrepancy in the lightcurves for the different energy thresholds is explained by looking at the 10 kpc CCSN event spectrum for JUNO again (Fig. 3.6) and seeing that at 0.20 MeV $\sim$ 10 events are expected over the whole CCSN. Hence, the difference the energy threshold makes is almost non-existent in an interval of a few ms around the burst.

Inverse beta decay

The inverse beta decay channel shows a few specific features.

First of all, in the early stages of the CCSN, only ν_e are emitted, making it then impossible for IBD events to be recorded in JUNO. And secondly, the 0.1 MeV energy threshold to qualify for a detectable event in JUNO has no influence on the IBD event spectrum as its threshold energy is $\sim$ 1.8 MeV.

As shown in the plots in Fig. 4.8, the IBD signal starts at $\sim$ 4 ms, which is the moment when $\bar{\nu}_e$ start to be created in the CCSN and escape of the interior of the star (Fig. 2.3).

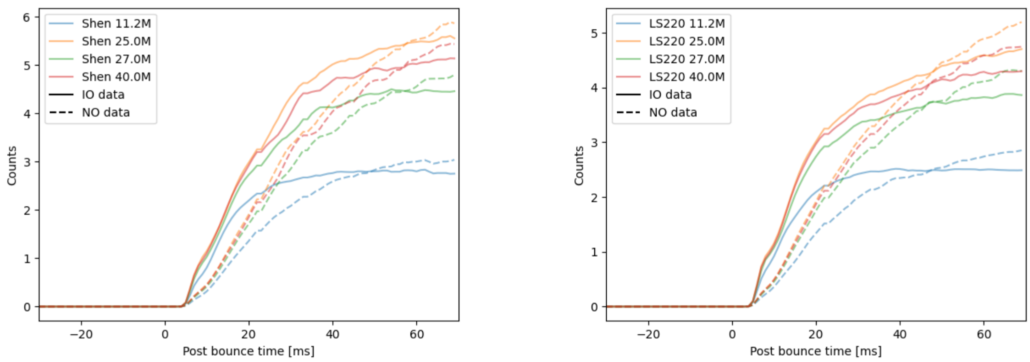

(a) Shen EoS

(b) LS EoS

Figure 4.8: Lightcurves for the IBD interaction channel for both EoS using the Garching group numerical model and for different progenitor masses. The CCSN is taken to be at 10 kpc.

Concerning the NMO discrimination, the IBD signal shows a certain NMO-sensitivity. Firstly, the IO signal rise is constantly steeper than the NO signal. Secondly, quite some time after the ν_e burst at around $\sim$ 40 ms depending on the mass, the IO and the NO curves intersect and the behaviours are swapped.

The difference in rise slopes and the behaviour swap are reliable tools for the NMO discrimination as they are dependent on the shape of the curve and not overall statistics, which would be influenced by mass, distance, model, etc.

Chapter 5

Statistical tools & methods for the NMO determination

This chapter presents the statistical methods and tools that will be used in the last section of this work to compute JUNO's sensitivity to the NMO based on CCSN neutrino signals. It starts by briefly putting back into context the general motivation for the study of lightcurves, then it introduces the χ^2-Poisson test and finally the toy Monte Carlo and Asimov methods are discussed in the general context of JUNO's NMO sensitivity.

5.1 Context & motivation

It is now clear that the lightcurves contain NMO information, lightcurves show NMO-dependent behaviours. In practice, the determination of the NMO is thus a matter of fitting an experimental spectrum to the expected spectrum of each NMO and judging which spectrum the experimental data best fits.

Sadly, there doesn't exist a reliable experimental way to observe CCSNe on command, which means that finding real experimental CCSN neutrino spectra to fit to the expected CCSN neutrino spectra and determine the NMO is not possible, and needs to rely on a pattern dependent on the parameters previously discussed. Therefore, rather than fitting experimental data and directly drawing conclusions on the NMO, the challenge is to compute how sensitive JUNO would be to the NMO discrimination when a CCSN actually comes, ultimately predicting with a certain confidence level how effective the JUNO experiment is in discerning the NMO based on CCSN neutrino signals.

To compute the NMO sensitivity of JUNO, experimental conditions are imitated through two statistical methods, both based on a χ^2 test : the Asimov method and the toy Monte Carlo method.

5.2 The χ^2-Poisson test

The NMO discrimination power of JUNO will be assessed through a minimum χ^2 test. The χ^2 test will be computed for the IO and NO hypotheses. The likelihood ratio between the two hypothesis will be the final test statistics. The χ^2 test is constructed based on a Poisson likelihood ratio function that asymptotically approaches a χ^2 distribution [55]. Indeed, the entries in the histogram's 1 ms bins are predicted to be relatively small and when considering an experimental lightcurve they are taken to follow a Poisson distribution, defined by the expected number of entries.

Let's thus examine the goodness of fit problem of a histogram with a range of N bins, an NMO-dependent expected number of events $\mu_i(\text{NMO})$ for each bin i and considering that the number of experimentally measured events in each bin n_i follows a Poisson distribution with mean $\mu_i(\text{NMO})$. The likelihood function of this histogram can be written as [56]

$$L(n_i;\mu_i(\text{NMO})) = \prod_{i=1}^{N} \mu_i(\text{NMO})^{n_i} \frac{e^{-\mu_i(\text{NMO})}}{n_i!} \tag{5.1}$$

Here the likelihood function can be divided by its maximum value $L(n_i;n_i)$ which is the likelihood function where the same n_i are measured but n_i is indeed expected [56]. This gives the Poisson likelihood ratio Λ

$$\Lambda = \frac{L(n_i;\mu_i(\text{NMO}))}{L(n_i;n_i)} \tag{5.2}$$

Assuming a NMO for the expected values μ_i and dropping the (NMO) in the equation, the negative log-likelihood ratio χ^2_Λ can be written as

$$\begin{aligned}
\chi^2_\Lambda(\text{NMO}) &= -2\ln\left[\frac{L(n_i;\mu_i)}{L(n_i;n_i)}\right] && (5.3)\\
&= -2\left(\ln L(n_i;\mu_i) - \ln L(n_i;n_i)\right) && (5.4)\\
&= -2\left(\sum_{i=1}^{N}\ln\left[\mu_i^{n_i}\frac{e^{-\mu_i}}{n_i!}\right] - \sum_{i=1}^{N}\ln\left[n_i^{n_i}\frac{e^{-n_i}}{n_i!}\right]\right) && (5.5)\\
&= -2\left(\sum_{i=1}^{N} n_i\ln\mu_i - \mu_i - \ln n_i! - \left(\sum_{i=1}^{N} n_i\ln n_i - n_i - \ln n_i!\right)\right) && (5.6)\\
&= -2\sum_{i=1}^{N} n_i - \mu_i + n_i\ln\left(\frac{\mu_i}{n_i}\right) && (5.7)
\end{aligned}$$

Wilks' theorem states that when minimizing χ^2_Λ with respect to the NMO (either IO or NO) through the expected data μ_i, χ^2_Λ asymptotically follows a non-central χ^2 distribution with one degree of freedom [57], which is the square of a standard normal distribution.

$$\chi^2_\Lambda \sim \chi^2_1 \tag{5.8}$$

Considering one data sample n_i, the NMO discrimination sensitivity is computed through the difference between the χ^2_Λ fit to both NMOs

$$\Delta\chi^2 = \left|\chi^2_\Lambda(\text{IO}) - \chi^2_\Lambda(\text{NO})\right| = \left|\chi^2(\text{IO}) - \chi^2(\text{NO})\right| \tag{5.9}$$

where

$$\chi^2_\Lambda(\text{NO}) = -2\sum_{i=1}^{N} n_i - \mu_i(\text{NO}) + n_i \ln\left(\frac{\mu_i(\text{NO})}{n_i}\right) \tag{5.10}$$

$$\chi^2_\Lambda(\text{IO}) = -2\sum_{i=1}^{N} n_i - \mu_i(\text{IO}) + n_i \ln\left(\frac{\mu_i(\text{IO})}{n_i}\right) \tag{5.11}$$

The fact that $\chi^2_\Lambda \sim \chi^2_1$ means that, if the inverse NMO is assumed for example, one can conclude based on the data sample n_i, that the IO can be excluded with certainty $\sqrt{\Delta\chi^2}\,\sigma$, where σ is the unit for the confidence level in terms of standard Gaussian deviation [57].

In the sections that follow, the Λ subscript for the χ^2 is considered implicit. To summarize, the complete expression for the χ^2 being fit to NMO', possibly based on measurements generated as following the NMO is written as

$$\chi^2(\text{NMO};\text{NMO}') = -2\sum_{i=1}^{N} n_i(\text{NMO}) - \mu_i(\text{NMO}') + n_i(\text{NMO}) \ln\left(\frac{\mu_i(\text{NMO}')}{n_i(\text{NMO})}\right) \tag{5.12}$$

Sometimes, the NMO-dependence is be dropped from the notation for readability when it is obvious in a given context.

Lastly, as in this work complete lightcurves are considered, one must always consider the combination of the three interaction channels' events and thus add a sum over the interaction channels c

$$\chi^2 = -2\sum_{c}\sum_{i=1}^{N} n_i - \mu_i + n_i \ln\left(\frac{\mu_i}{n_i}\right) \tag{5.13}$$

The two methods that are used in this work to compute the NMO sensitivity of JUNO, the toy Monte Carlo method and Asimov method, differ from each other in the way the data sets n_i are defined and how they compute JUNO's expected or median sensitivity.

5.2.1 Asimov method

The Asimov method aims to assess the expected NMO sensitivity of JUNO by replacing the measurements with the expected values of the experiment [58], which are in this case the expected number of entries per bin of the histogram for a determined NMO. This set of expected values, called the Asimov data set, puts the test in a kind of ideal case where the prediction of the lightcurve shape is perfectly accurate and one of two results are possible:

- **The assumed NMO is correct:** The χ^2 test is strictly equal to zero, which is expected as the χ^2 test compares two spectra that are strictly identical ($n_i = \mu_i(\text{NMO})$): $\chi^2(\text{NMO}) = -2\sum_c \sum_{i=1}^N \mu_i - \mu_i + \mu_i \ln\left(\frac{\mu_i}{\mu_i}\right) = 0$

- **The assumed NMO is incorrect, NMO' is correct:** The χ^2 test is not equal to zero and shows how sensitive the experiment is to the discrimination of the corresponding NMO by comparing the two expected spectra ($n_i = \mu_i(\text{NMO}')$): $\chi^2(\text{NMO}') = -2\sum_c \sum_{i=1}^N \mu_i(\text{NMO}') - \mu_i(\text{NMO}) + \mu_i(\text{NMO}') \ln\left(\frac{\mu_i(\text{NMO})}{\mu_i(\text{NMO}')}\right)$

The Asimov method thus measures the sensitivity of JUNO to the discrimination of the NMO in the cases of the NMO being inverse or normal, based on the difference in expected spectrum they have respective to each other. The sensitivity computed with the Asimov method, can also be quantified with the units of Gaussian deviation through the same relation as mentioned before [58]:

$$\sqrt{\Delta\chi^2} = \sqrt{\chi^2(\mathrm{NMO}') - \underbrace{\chi^2(\mathrm{NMO})}_{=0}} = \sqrt{\chi^2(\mathrm{NMO}')}\,\sigma. \tag{5.14}$$

However, the Asimov method, or more generally the χ^2 test, is based on the fact that the experimental spectrum's timeline can be perfectly superimposed on that of the spectrum it is being fit to. In other words, the origins of both spectra have to be perfectly known in order for the test to give a consistent sensitivity. When looking at the experimental setup of a CCSN observation, it becomes apparent that there are uncertainties when determining the bounce time $t = 0$ of the measured lightcurve and that it cannot be determined exactly. This uncertainty about the bounce time will reduce the overall NMO determination sensitivity of JUNO.

The uncertainty on the bounce time, i.e. on the start time of the signal window, is taken into account in the χ^2 test by simply considering the worst case scenario. A time shift Δt is added as fitting parameter to the χ^2 test, this time shift is applied to the expected number of events, with respect to the true bounce time (set at $t = 0$) and eventually the χ^2 test is minimized over the possible time shifts. This minimization will lead to a situation where the expectation shifted of Δt fits better the data set, hence accounting for a realistic situation where the bounce time will not be accurately known a priori, and the search window start will have an uncertainty which may lead to a "fake" better NMO sensitivity.

Considering for example the sensitivity of JUNO to the determination of the NMO when the IO is assumed (expected) but the neutrinos follow a NO (true), the Asimov method with Δt minimization works as follows:

1. The general χ^2 is set up with $n_i = \mu_i(\mathrm{NO})$ and $\mu_i = \mu_i(\mathrm{IO})$ (NMO dependence is dropped in the equation for readability):
   $\chi^2(\mathrm{NO};\mathrm{IO}) = -2\sum_c \sum_{i=1}^N n_i - \mu_i + n_i \ln\left(\frac{\mu_i}{n_i}\right)$
2. The time shift Δt is added to the expected data and the minimum χ^2 is computed to find the so-called worst case scenario regarding the calibration of the bounce time:
   $\chi^2_{\mathrm{min}}(\mathrm{NO};\mathrm{IO}) = -2\sum_c \sum_{i=1}^N n_i - \mu_i(\Delta t) + n_i \ln\left(\frac{\mu_i(\Delta t)}{n_i}\right)$
3. The sensitivity to the determination of the NMO, assuming initially an IO, of JUNO is computed via the relation previously mentioned: $\sqrt{\chi^2_{\mathrm{min}}(\mathrm{NO};\mathrm{IO})}\,\sigma$

5.2.2 Toy Monte Carlo method

One way of assessing the sensitivity of the $\Delta\chi^2$ test is through a Monte Carlo approach with the toy Monte Carlo method [59]. The toy Monte Carlo method relies on generating pseudo CCSNe or so-called pseudo-experiments by randomly sampling values from the Poisson distribution with as mean the expected number of entries, for each bin:

$$n_i \sim \mathrm{Pois}(\mu_i) \quad , i = 1, \ldots, N \tag{5.15}$$

The method consists of 5 steps:

1. With the Asimov method and for the same reasons as explained in the previous section, the Δt shift for which the χ^2(NMO) is minimum is computed for both NMOs, yielding two time shifts Δt(IO) and Δt(NO).

2. For each NMO a large number N of pseudo-experiments are generated through random Poisson sampling of the expected number of entries per bin. This results in 2 data sets of pseudo-experiments of equal size N, one data set per NMO.

3. The minimum χ^2 is computed for each of those pseudo-experiments, with the NMO data being minimized with respect to the time delay Δt(NMO). The four following χ^2 values are computed, for each pseudo-experiment, and each Δt:

   (a) N values for the NO data sets fit to the NO expected values: $\chi^2(\mathrm{NO};\mathrm{NO})$
   (b) N values for the NO data sets fit to the IO expected values: $\chi^2(\mathrm{NO};\mathrm{IO})$
   (c) N values for the IO data sets fit to the NO expected values: $\chi^2(\mathrm{IO};\mathrm{NO})$
   (d) N values for the IO data sets fit to the IO expected values: $\chi^2(\mathrm{IO};\mathrm{IO})$

4. Two different $\Delta\chi^2$ are computed, one for each NMO :

   (a) $\Delta\chi^2(\mathrm{IO}_{\mathrm{true}}) = \chi^2(\mathrm{IO};\mathrm{IO}) - \chi^2(\mathrm{IO};\mathrm{NO})$
   (b) $\Delta\chi^2(\mathrm{NO}_{\mathrm{true}}) = \chi^2(\mathrm{NO};\mathrm{NO}) - \chi^2(\mathrm{NO};\mathrm{IO})$

5. The medians of those two $\Delta\chi^2$ distribution are computed. These medians represent the expected experimental sensitivity of JUNO for the NMO discrimination. The experimental sensitivity, as for the Asimov method, is NMO-specific: the median of $\Delta\chi^2$(IO) represents the NMO sensitivity of JUNO if neutrinos follow an inverse NMO, and $\Delta\chi^2$(NO) if they follow a normal NMO. In units of Gaussian deviation the sensitivity is computed as $\sqrt{\Delta\chi^2}\,\sigma$

Chapter 6

Sensitivity to the NMO determination with CCSN neutrinos: results

This chapter discusses the application of the statistical methods developed in Chapter 5 to the simulated lightcurves described in Chapter 4 in order to assess the NMO discrimination power of JUNO. It begins by discussing the Asimov method's results and performance in function of certain parameters, followed by a similar discussion for the toy Monte Carlo method.

6.1 Asimov method : discussion & results

6.1.1 Set-up

The Asimov method relies heavily on the model used of the expected lightcurve, for each NMO. As it has been discussed in Chapter 4, several parameters induce noticeable differences in lightcurves, which can eventually lead to a different expected sensitivity in JUNO and must therefore be avoided. The purpose of this section is to take these parameters that may impact the results into account in order to yield robust and consistent sensitivity values.

First, the fact that CCSNe are not well understood has repercussions on the conclusions that the Asimov method, and other statistical tests, can draw about the NMO sensitivity of JUNO. Indeed, lightcurves show some model dependency (cf. Section 4.3.3) and as no model is taken to be more accurate than the other, the sensitivity in case an explosion occurs will depend on the correct model and progenitor star characteristics. As the model dependence seems to be stronger after the neutrino burst (Fig 4.4), it is sensible to focus on the neutronization burst only in order to avoid as much as possible that model dependency.

Secondly, the progenitor mass also has an influence on the lightcurve which leads to big differences in the number of observed events, specially in the accretion phase (Fig 4.2). The progenitor mass can obviously not be chosen when observing a CCSN but the lightcurve mass dependency can be avoided by focussing on a short time window from the start of the signal.

Based on the different plots of Chapter 4, the overall mass-model dependency of the lightcurves has thus been qualitatively assessed to be important starting from ~ 20 ms after the bounce. Thus, limiting the χ^2 analysis range (number of bins N considered for the χ^2) to a range around the bounce would remove some of the mass-model dependency of the measured signal. The plots in Fig. 6.1 illustrate the mass-model dependency of the Asimov method by plotting the computed sensitivity $\Delta\chi^2$ as a function of the end of the time window for a fixed starting time of -20 ms, with respect to the bounce time at $t = 0$ ms.

For both NMOs and all progenitor masses of the CCSN, the computed sensitivities seem to be spread out the bigger the time window is. The spreading out of the sensitivities becomes too consequential starting from $t_{\max} = 20$ ms, as is more precisely illustrated in Fig. 6.2. For the rest of this chapter, the time window for the Asimov method is thus assumed to be $[-20; 20]$ ms.

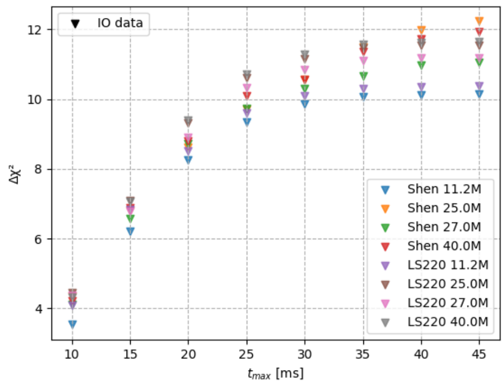

(a) IO scenario

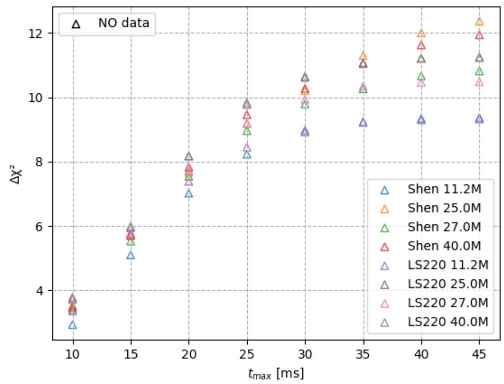

(b) NO scenario

Figure 6.1: NMO sensitivity of JUNO computed with the Asimov method for a CCSN at 10kpc, in function of the time window ending time $t_{\max}$ considering a fixed starting time of $t_{\min} = -20$ ms

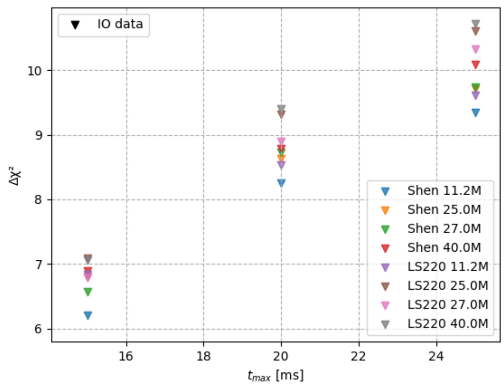

(a) IO scenario

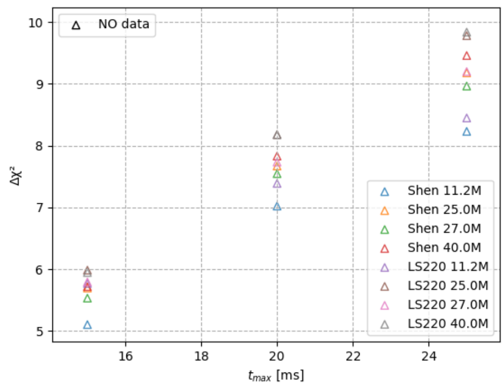

(b) NO scenario

Figure 6.2: Zoomed in plot of Fig. 6.1, showing more clearly the sensitivities getting too spread out for time windows ending after 20 ms.

6.1.2 Benchmark result

As a pseudo-reference sensitivity test, the Asimov method has first been applied to a very generic CCSN observation scenario: a 27 $M_\odot$ CCSN at a distance of 10 kpc described by the Shen EoS. The expected lightcurves are represented below in Fig. 6.3.

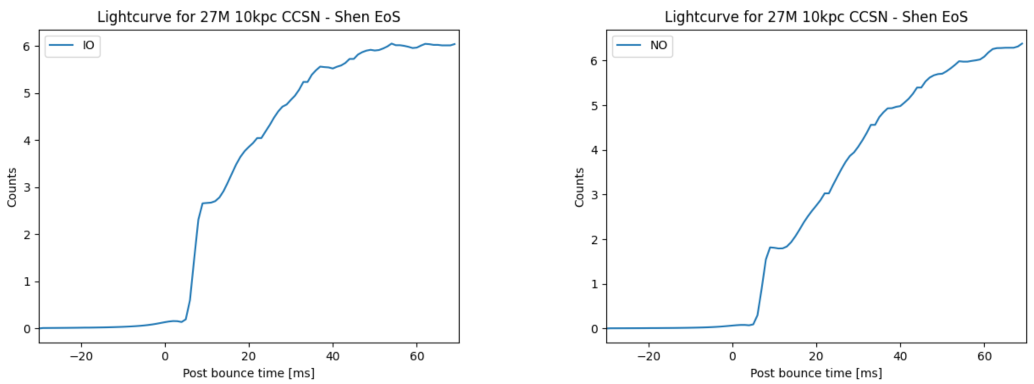

(a) IO scenario (b) NO scenario

Figure 6.3: Expected lightcurve for each NMO given a 27 $M_\odot$ CCSN at 10kpc

For the determination of the NMO in case IO is the true hypothesis (IO data) when neutrinos are expected to follow the NO, the Asimov method reports a sensitivity of $\chi^2_{\text{min}}(\text{IO}) = 8.73$ or $\sqrt{\chi^2_{\text{min}}(\text{IO})} = 2.95\,\sigma$, which is consistent with Fig. 6.2a, and $\Delta t = +2$ ms as the time shift that when applied to the IO lightcurve makes it resemble the most to the NO lightcurve. Just as expected, when comparing the IO data with the IO alternative hypothesis, the minimum χ^2 test finds a minimum at a time shift $\Delta t = 0$ ms which yields a strict zero sensitivity $\sqrt{\chi^2_{min}} = 0$ as in this situation the χ^2 is comparing two identical spectra which are indeed indistinguishable when they are overlapped with the same bounce time as reference. The $\chi^2(\text{IO})$ distribution with respect to Δt is plotted in Fig. 6.4a and in Fig. 6.4b a parabolic is applied to the distribution. The parabolic fit not being very satisfactory comes from the fact that strictly speaking $\chi^2 \sim -2\ln\Lambda$, which only has a parabolic shape in the Gaussian limit of the data distribution and therefore here in the Poisson limit the χ^2 deviates from the perfect parabolic shape [56].

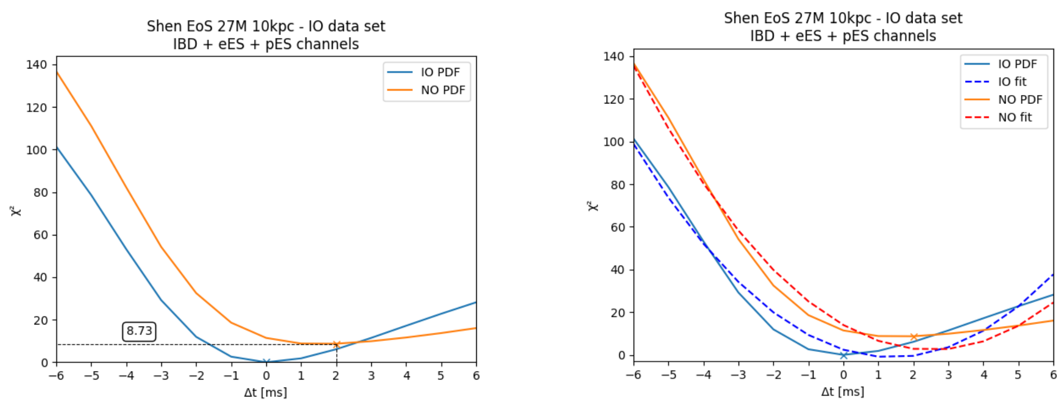

(a) Asimov χ^2 minimization w.r.t Δt (b) Parabolic fit applied to $\chi^2(\Delta t)$.

Figure 6.4: Δt minimization with the Asimov method, given a NO data set $n_i = \mu_i(\text{IO})$

In the case of the NMO determination based on NO data and assuming an IO nature, the sensitivity of JUNO is slightly worse. The Asimov method yields a sensitivity of $\chi^2_{\text{min}}(\text{NO}) = 7.55$ or $\sqrt{\chi^2_{\text{min}}(\text{NO})} = 2.74\,\sigma$ with a negative time shift $\Delta t = -1$ ms. The negative time shift is consistent with the fact that when shifting an IO spectrum to fit a NO spectrum, the shift is positive, and thus the time shift is negative when fitting an NO spectrum to an IO spectrum.

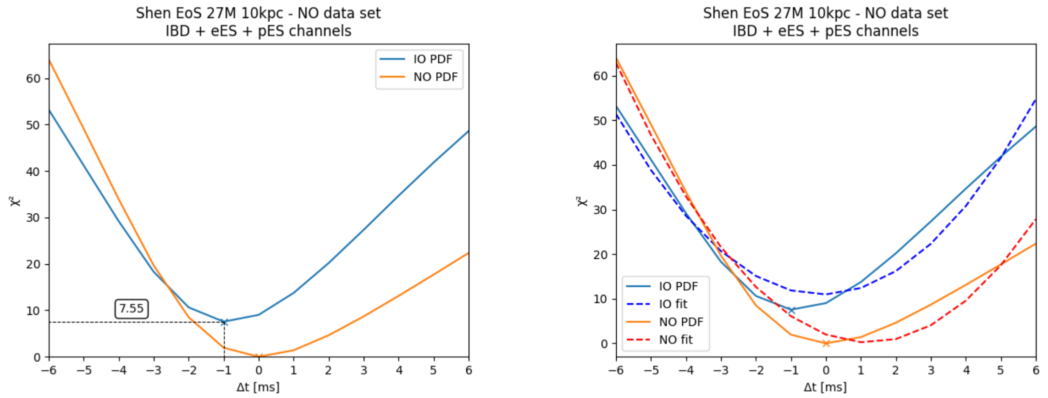

(a) Asimov χ^2 minimization w.r.t Δt (b) Parabolic fit applied to $\chi^2(\Delta t)$.

Figure 6.5: Δt minimization with the Asimov method, given a NO data set $n_i = \mu_i(\text{NO})$

As for the LS EoS, it produces similar results as can be seen in Fig. 6.6

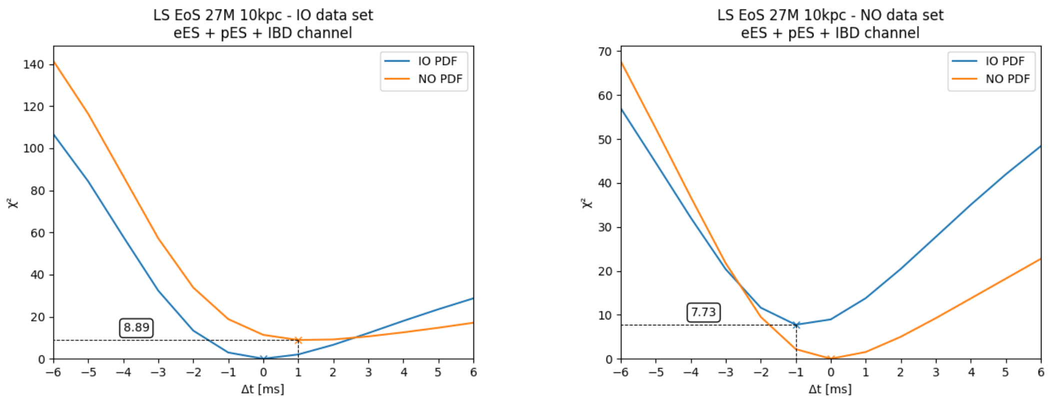

(a) IO scenario (b) NO scenario

Figure 6.6: Δt minimization with the Asimov method given different NMO data sets for CCSNe described by the LS EoS.

6.1.3 Sensitivity of the interaction channels

Each interaction channel, on their own, shows very little sensitivity to the NMO discrimination as the overall number of events around the bounce are quite low, thus weakening the overal statistical test. A few things can however still be noted. The strict zero sensitivity of the pES channel is expected as the pES channel is a colorless interaction with no flavor sensitivity, hence no NMO sensitivity (cf. Section 4.3.4). Next, the eES channel being not very sensitive to the NMO is consistent with the fact that the NMO difference in the eES lightcurves comes in the form of an overall scaling bringing no shape difference and the fact that the eES represents a very low statistics.

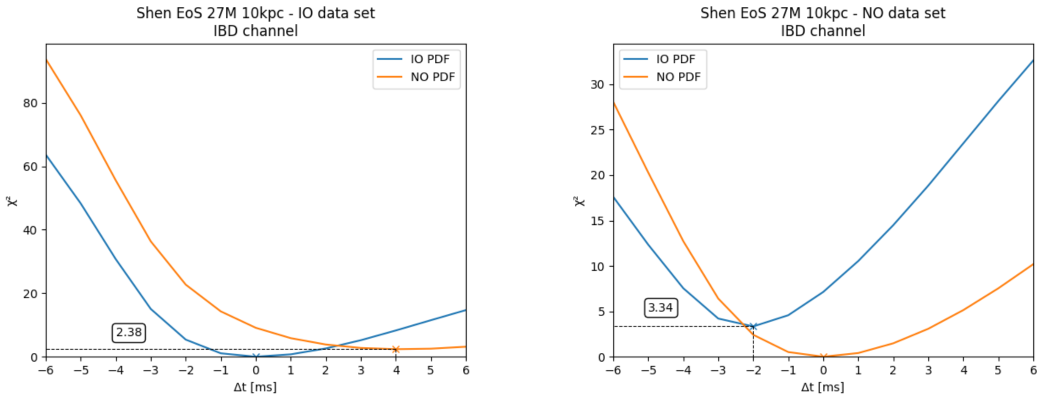

(a) IO data $n_i = \mu_i(\text{IO})$ (b) NO data $n_i = \mu_i(\text{NO})$

Figure 6.7: Asimov method applied to the IBD interaction channel for both NMOs.

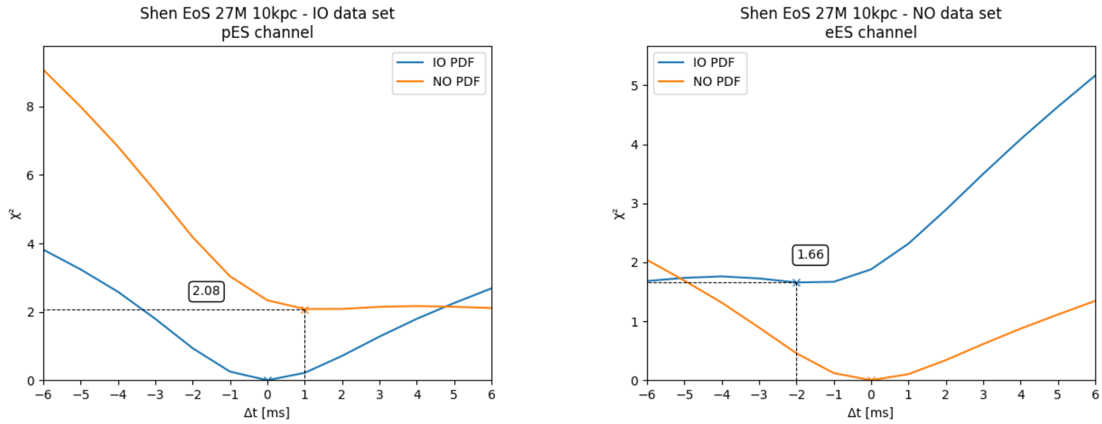

(a) IO data $n_i = \mu_i(\text{IO})$ (b) NO data $n_i = \mu_i(\text{NO})$

Figure 6.8: Asimov method applied to the eES interaction channel for both NMOs.

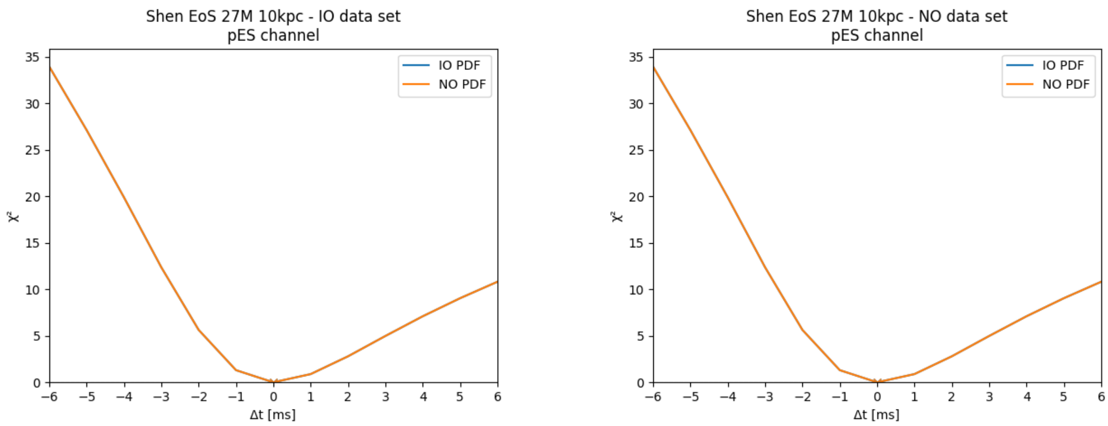

(a) IO data $n_i = \mu_i(\text{IO})$ (b) NO data $n_i = \mu_i(\text{NO})$

Figure 6.9: Asimov method applied to the pES interaction channel for both NMOs.

6.1.4 Impact of the distance

The distance d of a CCSN influences the number of events recorded by JUNO with a factor of $\frac{1}{d^2}$, this scales the lightcurve as was shown in Fig. 4.3a and 4.3b. Starting from the $\frac{1}{d^2}$ scaling of the number of events, one shows that the sensitivity follows a $\frac{1}{d^2}$ scaling too:

$$\chi^2(d) = -2\sum_c \sum_{i=1}^{N} n_i \cdot \frac{1}{d^2} - \mu_i \cdot \frac{1}{d^2} + n_i \cdot \frac{1}{d^2} \ln\left(\frac{\mu_i \cdot \frac{1}{d^2}}{n_i \cdot \frac{1}{d^2}}\right) \tag{6.1}$$

$$= -2 \cdot \frac{1}{d^2} \cdot \sum_c \sum_{i=1}^{N} n_i - \mu_i + n_i \ln\left(\frac{\mu_i}{n_i}\right) = \chi^2 \cdot \frac{1}{d^2} \tag{6.2}$$

This scaling is illustrated in the plots in Fig. 6.10 where the sensitivity is fit to a $\frac{1}{d^2}$ curve for both NMOs. In the plot of Fig. 6.10b the distances for which the NMO sensitivity is at least 3 or 5σ are indicated with the black dashed line. One concludes based on this plot and assuming the Shen EoS, that for a 27 $M_\odot$ CCSN JUNO discriminates either NMOs with a 3 (5) σ confidence level for CCSNe closer than ~ 10 (7) kpc.

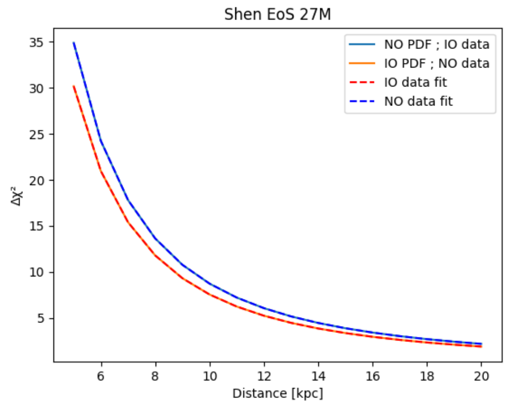

(a) Sensitivity $\Delta\chi^2$

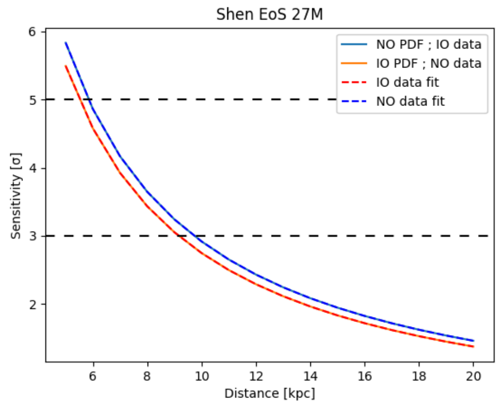

(b) Sensitivity with the 3 and $5\,\sigma$ threshold in the dashed black line

Figure 6.10: Sensitivity in different units for both NMOs, in function the CCSN distance.

6.2 Toy Monte Carlo method: discussion & results

6.2.1 Poisson fluctuating lightcurves

The toy Monte Carlo implements Poisson fluctuations of the expected number of events in each of the lightcurve's bins to simulate an experimental situation (Eq. 5.15). The lightcurves with Poisson fluctuations are plotted in Fig. 6.11 for both NMOs.

The Poisson fluctuations naturally lead to spectra that are harder to tell apart than in the ideal case of the Asimov method. The toy Monte Carlo method is thus expected to yield slightly worse sensitivities than the Asimov method.

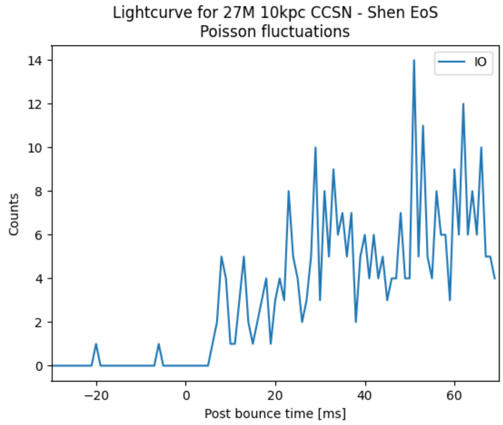

(a) IO scenario

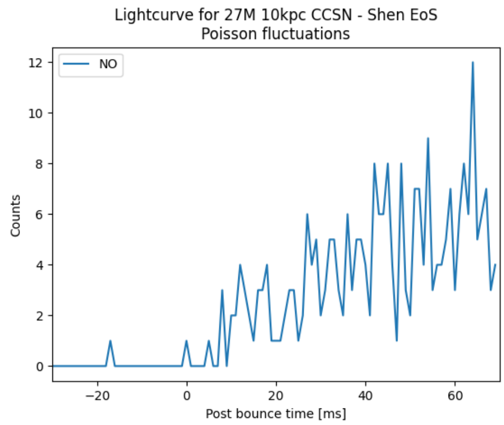

(b) NO scenario

Figure 6.11: Lightcurves with Poisson fluctuations for a $27\,M_\odot$ CCSN at 10 kpc described by the Shen EoS.

6.2.2 Minimization over Δt

For the reasons listed in Sections 5.2.1 and 5.2.2, the toy Monte Carlo method implements a minimization over the time shifts Δt to compute a sensitivity in a worst case scenario regarding the bounce time calibration. There are two ways to proceed to apply the Δt minimization for the toy Monte Carlo method:

1. **Fixed time shift:** The χ^2 minimization over the Δt is computed through the Asimov method and then implemented in the $\Delta\chi^2$ test. This procedure thus uses a fixed Δt for the totality of the $\Delta\chi^2$ tests.

2. **Fluctuating time shift:** The χ^2 minimization over the Δt is individually computed for each pseudo-experiment and then implemented in each $\Delta\chi^2$ test. Thus, this procedures yields a fluctuating time shift Δt for each $\Delta\chi^2$ test.

Fixed time shift

For the fixed time shift method, the toy Monte Carlo method reports sensitivities of $\sqrt{|\Delta\chi^2(\mathrm{NO})|} = 2.79\,\sigma$ and $\sqrt{|\Delta\chi^2(\mathrm{IO})|} = 2.52\,\sigma$. These sensitivities are, as expected, worse than the sensitivities computed with the Asimov method, but show a peculiar EoS dependence. Indeed, when the Shen EoS is used the toy Monte Carlo method predicts that the NO is easier to discriminate than the IO, which is the opposite of what the Asimov method predicted (Fig. 6.4). However when the LS EoS is used, the test shows a bigger sensitivity to the IO, which was predicted by the Asimov method (Fig. 6.6), and an overall better performance.

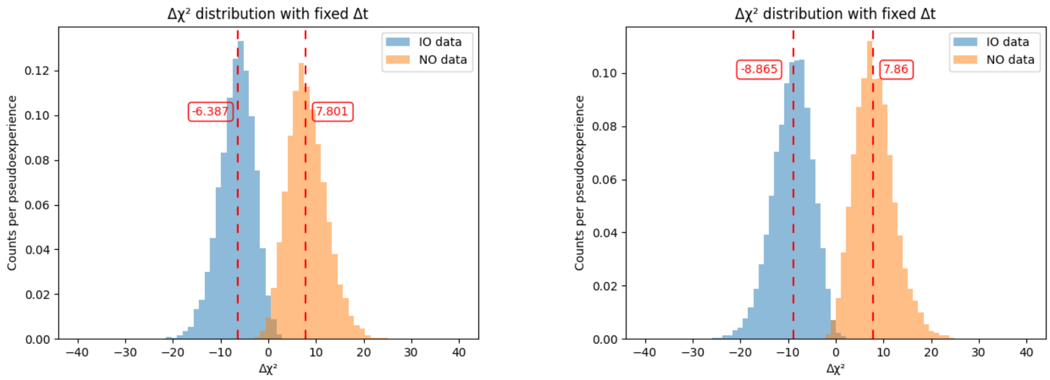

(a) Shen EoS (b) LS EoS

Figure 6.12: $\Delta\chi^2$ distributions for 10 000 pseudo-experiments of a 27 $M_\odot$ CCSN at 10 kpc, with the median indicated by the red dashed line.

Varying time shift

When the time shift Δt fluctuates as a result of the Poisson fluctuations as well, the results are not very promising. The median sensitivities as computed by the toy Monte Carlo method are listed in Table 6.1

	IO data	NO data
Shen EoS	$\Delta\chi^2 = -4.12$	$\Delta\chi^2 = 1.94$
LS EoS	$\Delta\chi^2 = -4.79$	$\Delta\chi^2 = 2.37$

Table 6.1: $\Delta\chi^2$ sensitivities computed with the toy Monte Carlo method with fluctuating Δt, for each EoS.

The values of the different sensitivities show that the toy Monte Carlo method predicts a significantly bigger sensitivity for the NMO discrimination in the IO case than in the NO case. Moreover, they show that the variation of the Δt leads to predict a very weak sensitivity to both NMOs.

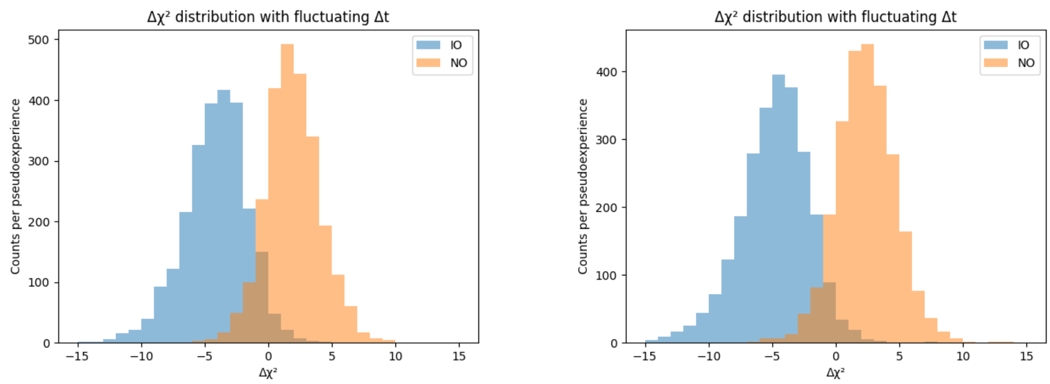

(a) Shen EoS (b) LS EoS

Figure 6.13: $\Delta\chi^2$ distributions for 2500 pseudo-experiments of a 27 $M_\odot$ CCSN at 10 kpc, with a fluctuating Δt minimization.

It is also interesting to look at the minimum Δt distribution the toy Monte Carlo method yields for the LS EoS (Fig. 6.15) and for the Shen EoS (Fig. 6.14).

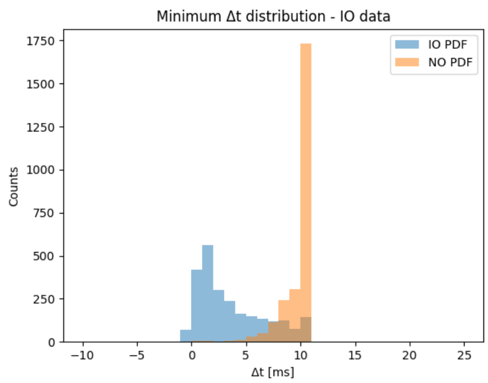

(a) IO scenario

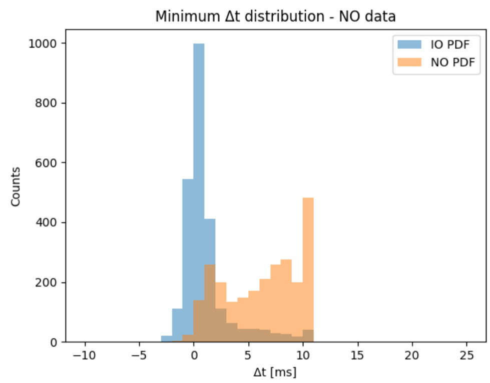

(b) NO scenario

Figure 6.14: Δt distributions as a result of the χ^2 minimization for 2500 pseudo-experiments of a 27 $M_\odot$ CCSN at 10 kpc described by the Shen EoS.

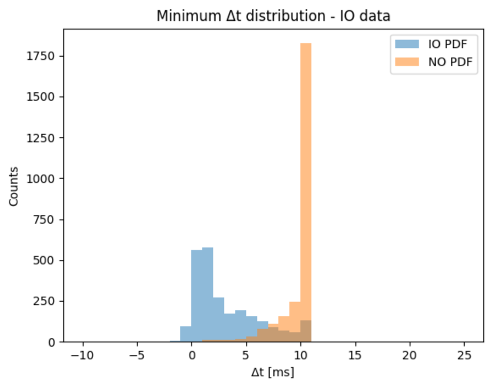

(a) IO scenario

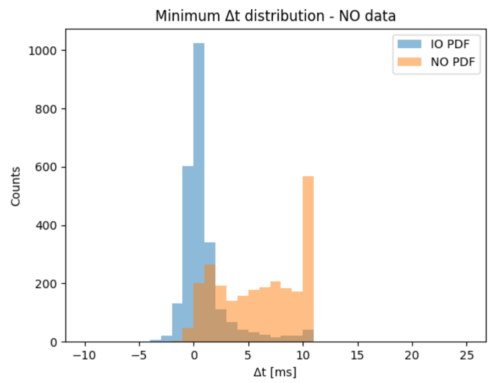

(b) NO scenario

Figure 6.15: Δt distributions as a result of the χ^2 minimization for 2500 pseudo-experiments of a 27 $M_\odot$ CCSN at 10 kpc described by the LS EoS.

Here, the toy Monte Carlo method shows mixed results.

The Δt distribution does not show a clear peaked distribution around $t = 0\,\text{ms}$ in the case where the assumed NMO (NMO PDF on the plots) is the correct NMO (NMO data on the plots). Instead the distributions show a small peak at $t = 0\,\text{ms}$ and a pronounced distribution tail in the IO case (Fig. 6.14a and 6.15a). In the NO case the Δt distribution is a plateau with a peak at $\Delta t = +10\,\text{ms}$ which is the highest possible Δt considered in the fit with the toy Monte Carlo simulations.

For the opposite situation, meaning when the wrong NMO is assumed, in the NO data case one observes a peak centered around $\Delta t = +1\,\text{ms}$ with some distribution tail just as expected. For the IO case however, a big peak can be seen for the biggest time shift $\Delta t = +10\,\text{ms}$ with a small tail distribution.

All in all, the Δt fluctuate too much using this method and it is thus hard to predict a consistent median sensitivity. A careful investigation of these results will be done.

Conclusion

In this work, CCSN lightcurves have been generated using the Garching group numerical model and based on the Shen or LS EoS. Next, a $\Delta\chi^2$ test based on the Poisson likelihood ratio has been constructed to apply the Asimov method and the toy Monte Carlo to the lightcurves in order to eventually compute the expected sensitivity of the JUNO experiment to the determination of the NMO.

In order to draw consistent conclusions regarding the said NMO sensitivity, the impact of the numerical model, the progenitor mass, the NMO, the CCSN distance and the different the interaction channels on both the lightcurves and the statistical methods have been assessed.

The uncertainty on the exact bounce time of an experimental lightcurve has also been considered and taken into account. For this, a time shift has been applied to the expected spectrum and a minimum χ^2 test over the possible time shifts was implemented in order to account for a realistic experimental situation where the bounce time would be calibrated in the worst way possible. This gives a conservative but robust measurement of the expected sensitivity.

When applied to the generic case of a $27\,\mathrm{M}_\odot$ CCSN at 10 kpc described by the Shen EoS, the Asimov method yields a sensitivity of $2.95\,\sigma$ in the IO case and $2.75\,\sigma$ in the NO case. The toy Monte Carlo method on the other hand, when a fixed Δt minimization is implemented, reports a sensitivity of $2.52\,\sigma$ in the IO case and $2.79\,\sigma$ in the NO case. When the Δt is implemented to fluctuate with each pseudo-experiment the toy Monte Carlo method reports a less satisfactory sensitivity of $2.02\ \sigma$ in the IO case.

Furthermore, expecting a discrimination power of at least $3\,\sigma$ has been assessed to be possible only for either relatively nearby CCSN, relatively massive progenitors and/or at the overall cost of the sensitivity being model dependent.

In order to draw a complete picture of the NMO sensitivity of JUNO with CCSN neutrinos, several perspectives could be considered.

First, not all interaction channels have been considered, the ^{14}C and ^{12}N interaction channels could be implemented in the lightcurves as well.

Other CCSN numerical models, such as the Bollig or Nakazato model can be investigated. Understanding how they work and how they influence the expected sensitivity could draw a clearer picture of the NMO sensitivity.

In this work, only lightcurves have been considered but the energy reconstruction and spectrum of CCSN neutrinos could also bring additional results and NMO information.

The neutrino detection in this work was considered perfect, the application of CCSN neutrino signals detection to the PMT response, electronic data acquisition system, background noise etc. should be assessed to get a complete view of the JUNO's experiment NMO sensitivity.

Bibliography

[1] John N. Bahcall and Raymond Davis. “Solar Neutrinos: A Scientific Puzzle”. In: *Science* 191.4224 (Jan. 23, 1976), pp. 264–267. ISSN: 0036-8075, 1095-9203. DOI: 10.1126/science.191.4224.264. URL: https://www.science.org/doi/10.1126/science.191.4224.264.

[2] B. Pontecorvo. “Mesonium and anti-mesonium”. In: *Sov. Phys. JETP* 6 (1957), p. 429.

[3] The Nobel Foundation. *The Nobel Prize in Physics 2015*. NobelPrize.org. URL: https://www.nobelprize.org/prizes/physics/2015/summary/ (visited on 07/26/2023).

[4] T. Adam et al. *JUNO Conceptual Design Report*. Sept. 28, 2015. DOI: 10.48550/arXiv.1508.07166. arXiv: 1508.07166[hep-ex,physics:physics]. URL: http://arxiv.org/abs/1508.07166.

[5] G. Aad et al. “Observation of a new particle in the search for the Standard Model Higgs boson with the ATLAS detector at the LHC”. In: *Physics Letters B* 716.1 (Sept. 2012), pp. 1–29. DOI: 10.1016/j.physletb.2012.08.020. URL: https://doi.org/10.1016%2Fj.physletb.2012.08.020.

[6] Ahmed Tarek Abouelfadl Mohamed. *The Standard Model of Particle Physics*. en. Ed. by Ahmed Tarek Abouelfadl Mohamed. Springer Theses. Cham: Springer International Publishing, 2020. ISBN: 978-3-030-59516-6. DOI: 10.1007/978-3-030-59516-6_1. URL: https://doi.org/10.1007/978-3-030-59516-6_1.

[7] V. N. Gavrin. “Contribution of gallium experiments to the understanding of solar physics and neutrino physics”. In: *Physics of Atomic Nuclei* 76.10 (Oct. 1, 2013), pp. 1238–1243. ISSN: 1562-692X. DOI: 10.1134/S106377881309007X. URL: https://doi.org/10.1134/S106377881309007X.

[8] Y. Et Al. Fukuda. “Evidence for Oscillation of Atmospheric Neutrinos”. In: *Physical Review Letters* 81 (Aug. 1, 1998), pp. 1562–1567. ISSN: 0031-9007. DOI: 10.1103/PhysRevLett.81.1562. URL: https://ui.adsabs.harvard.edu/abs/1998PhRvL..81.1562F.

[9] Nick Jelley et al. “The Sudbury Neutrino Observatory”. In: *Annual Review of Nuclear and Particle Science* 59.1 (Nov. 1, 2009), pp. 431–465. ISSN: 0163-8998, 1545-4134. DOI: 10.1146/annurev.nucl.55.090704.151550. URL: https://www.annualreviews.org/doi/10.1146/annurev.nucl.55.090704.151550.

[10] J. W. F. Valle. “Neutrino physics overview”. In: *Journal of Physics: Conference Series* 53 (Nov. 1, 2006), pp. 473–505. ISSN: 1742-6588, 1742-6596. DOI: 10.1088/1742-6596/53/1/031. arXiv: hep-ph/0608101. URL: http://arxiv.org/abs/hep-ph/0608101.

[11] Barbara Clerbaux. *Physique des particules - Chapitre VII. Les oscillations des neutrinos*. Université Libre de Bruxelles. 2022.

[12] Robert Mann. *An Introduction to Particle Physics and the Standard Model*. Taylor & Francis, 2010. ISBN: 978-1-4200-8300-2 978-1-4200-8298-2 978-0-429-14122-5. DOI: 10.1201/9781420083002. URL: https://directory.doabooks.org/handle/20.500.12854/72208.

[13] Fengpeng An et al. "Neutrino physics with JUNO". In: *Journal of Physics G: Nuclear and Particle Physics* 43.3 (Feb. 2016), p. 030401. DOI: 10.1088/0954-3899/43/3/030401. URL: https://doi.org/10.1088%2F0954-3899%2F43%2F3%2F030401.

[14] K. Abe et al. "Atmospheric neutrino oscillation analysis with external constraints in Super-Kamiokande I-IV". In: *Physical Review D* 97.7 (Apr. 2018). DOI: 10.1103/physrevd.97.072001. URL: https://doi.org/10.1103%2Fphysrevd.97.072001.

[15] Borexino Collaboration et al. "Final results of Borexino Phase-I on low-energy solar neutrino spectroscopy". In: *Physical Review D* 89.11 (June 25, 2014). Publisher: American Physical Society, p. 112007. DOI: 10.1103/PhysRevD.89.112007. URL: https://link.aps.org/doi/10.1103/PhysRevD.89.112007.

[16] R. L. Workman et al. "Review of Particle Physics". In: *PTEP* 2022 (2022), p. 083C01. DOI: 10.1093/ptep/ptac097.

[17] M. A. Acero et al. "Improved measurement of neutrino oscillation parameters by the NOvA experiment". In: *Physical Review D* 106.3 (Aug. 2022). DOI: 10.1103/physrevd.106.032004. URL: https://doi.org/10.1103%2Fphysrevd.106.032004.

[18] Hyper-Kamiokande Proto-Collaboration et al. *Hyper-Kamiokande Design Report*. 2018. arXiv: 1805.04163 [physics.ins-det].

[19] "JUNO physics and detector". In: *Progress in Particle and Nuclear Physics* 123 (Mar. 2022), p. 103927. DOI: 10.1016/j.ppnp.2021.103927. URL: https://doi.org/10.1016%2Fj.ppnp.2021.103927.

[20] Michelle J. Dolinski et al. "Neutrinoless Double-Beta Decay: Status and Prospects". In: *Annual Review of Nuclear and Particle Science* 69.1 (Oct. 2019), pp. 219–251. DOI: 10.1146/annurev-nucl-101918-023407. URL: https://doi.org/10.1146%2Fannurev-nucl-101918-023407.

[21] JUNO Collaboration et al. *JUNO sensitivity to the annihilation of MeV dark matter in the galactic halo*. Aug. 10, 2023. arXiv: 2306.09567[astro-ph,physics:hep-ex,physics:hep-ph]. URL: http://arxiv.org/abs/2306.09567.

[22] S Gariazzo et al. "Light sterile neutrinos". In: *Journal of Physics G: Nuclear and Particle Physics* 43.3 (Mar. 2015), p. 033001. DOI: 10.1088/0954-3899/43/3/033001. URL: https://doi.org/10.1088%2F0954-3899%2F43%2F3%2F033001.

[23] S. E. Woosley et al. "The evolution and explosion of massive stars". In: *Reviews of Modern Physics* 74 (Nov. 1, 2002), pp. 1015–1071. ISSN: 0034-6861. DOI: 10.1103/RevModPhys.74.1015. URL: https://ui.adsabs.harvard.edu/abs/2002RvMP...74.1015W.

[24] Anwar Kamal. *Nuclear Physics*. Graduate Texts in Physics. Berlin, Heidelberg: Springer, 2014. ISBN: 978-3-642-38654-1 978-3-642-38655-8. DOI: 10.1007/978-3-642-38655-8. URL: https://link.springer.com/10.1007/978-3-642-38655-8.

[25] D Koester and G Chanmugam. "Physics of white dwarf stars". In: *Reports on Progress in Physics* 53.7 (July 1, 1990), pp. 837–915. ISSN: 0034-4885, 1361-6633. DOI: 10.1088/0034-4885/53/7/001. URL: https://iopscience.iop.org/article/10.1088/0034-4885/53/7/001.

[26] Chris Impey. *Astronomy - State of the Art - Stars*. 2014. URL: https://www.slideshare.net/chrisimpey1/4-slidesstars.

[27] H. A. Bethe. "Supernova mechanisms". In: *Reviews of Modern Physics* 62.4 (Oct. 1, 1990), pp. 801–866. DOI: 10.1103/RevModPhys.62.801. URL: https://link.aps.org/doi/10.1103/RevModPhys.62.801.

[28] Hans-Thomas Janka. "Neutrino Emission from Supernovae". In: *Handbook of Supernovae*. Springer International Publishing, 2017, pp. 1575–1604. DOI: 10.1007/978-3-319-21846-5_4. URL: https://doi.org/10.1007%2F978-3-319-21846-5_4.

[29] M. Kachelrieß et al. "Exploiting the neutronization burst of a galactic supernova". In: *Physical Review D* 71.6 (Mar. 2005). DOI: 10.1103/physrevd.71.063003. URL: https://doi.org/10.1103%2Fphysrevd.71.063003.

[30] Heamin Ko et al. "Comprehensive Analysis of the Neutrino Process in Core-collapsing Supernovae". In: *The Astrophysical Journal* 937.2 (Oct. 2022). Publisher: The American Astronomical Society, p. 116. ISSN: 0004-637X. DOI: 10.3847/1538-4357/ac88cd. URL: https://dx.doi.org/10.3847/1538-4357/ac88cd.

[31] A. Yu Smirnov. "The MSW Effect and Matter Effects in Neutrino Oscillations". In: *Physica Scripta* 2005 (T121 Jan. 2005), p. 57. ISSN: 1402-4896. DOI: 10.1088/0031-8949/2005/T121/008. URL: https://dx.doi.org/10.1088/0031-8949/2005/T121/008.

[32] JUNO Collaboration et al. *The JUNO experiment Top Tracker*. 2023. arXiv: 2303.05172 [hep-ex].

[33] Angel Abusleme et al. "Sub-percent precision measurement of neutrino oscillation parameters with JUNO*". In: *Chinese Physics C* 46.12 (Dec. 2022). Publisher: Chinese Physical Society and the Institute of High Energy Physics of the Chinese Academy of Sciences and the Institute of Modern Physics of the Chinese Academy of Sciences and IOP Publishing Ltd, p. 123001. ISSN: 1674-1137. DOI: 10.1088/1674-1137/ac8bc9. URL: https://dx.doi.org/10.1088/1674-1137/ac8bc9.

[34] William J Marciano and Zohreh Parsa. "Neutrino–electron scattering theory". In: *Journal of Physics G: Nuclear and Particle Physics* 29.11 (Oct. 2003), pp. 2629–2645. DOI: 10.1088/0954-3899/29/11/013. URL: https://doi.org/10.1088%2F0954-3899%2F29%2F11%2F013.

[35] Asan Damanik. "Feynman amplitude for Dirac and Majorana neutrinos". In: *Electronic Journal of Theoretical Physics* 13 (May 2016), pp. 73–78.

[36] Alessandro Mirizzi et al. "Supernova Neutrinos: Production, Oscillations and Detection". In: *La Rivista del Nuovo Cimento* 39.102 (Feb. 5, 2016), pp. 1–112. ISSN: 0393697X, 0393697X. DOI: 10.1393/ncr/i2016-10120-8. arXiv: 1508.00785[astro-ph,physics:hep-ex,physics:hep-ph]. URL: http://arxiv.org/abs/1508.00785.

[37] John F. Beacom et al. “Detection of supernova neutrinos by neutrino-proton elastic scattering”. In: *Physical Review D* 66.3 (Aug. 2002). DOI: 10.1103/physrevd.66.033001. URL: https://doi.org/10.1103%2Fphysrevd.66.033001.

[38] A. A. Boyarchuk et al. “Observations with the "Astron" : supernova 1987A in the Large Magellanic Cloud.” In: *Pisma v Astronomicheskii Zhurnal* 13 (Sept. 1, 1987). ADS Bibcode: 1987PAZh...13..739B, pp. 739–743. ISSN: 0320-0108. URL: https://ui.adsabs.harvard.edu/abs/1987PAZh...13..739B.

[39] Kohsuke Sumiyoshi. “Equation of state and neutrino transfer in supernovae and neutron stars”. In: *The European Physical Journal A* 57.12 (Dec. 2021). DOI: 10.1140/epja/s10050-021-00644-z. URL: https://doi.org/10.1140%2Fepja%2Fs10050-021-00644-z.

[40] H. Shen et al. “Relativistic equation of state of nuclear matter for supernova and neutron star”. In: *Nuclear Physics A* 637.3 (July 1998), pp. 435–450. DOI: 10.1016/s0375-9474(98)00236-x. URL: https://doi.org/10.1016%2Fs0375-9474%2898%2900236-x.

[41] James M. Lattimer and F. Douglas Swesty. “A generalized equation of state for hot, dense matter”. In: *Nuclear Physics A* 535.2 (Dec. 16, 1991), pp. 331–376. ISSN: 0375-9474. DOI: 10.1016/0375-9474(91)90452-C. URL: https://www.sciencedirect.com/science/article/pii/037594749190452C.

[42] P.-G. Reinhard. “The relativistic mean-field description of nuclei and nuclear dynamics”. In: *Reports on Progress in Physics* 52.4 (Apr. 1989), p. 439. ISSN: 0034-4885. DOI: 10.1088/0034-4885/52/4/002. URL: https://dx.doi.org/10.1088/0034-4885/52/4/002.

[43] N.H. March. “The Thomas-Fermi approximation in quantum mechanics”. In: *Advances in Physics* 6.21 (Jan. 1, 1957), pp. 1–101. ISSN: 0001-8732. DOI: 10.1080/00018735700101156. URL: https://doi.org/10.1080/00018735700101156.

[44] Hans-Thomas Janka et al. “Physics of Core-Collapse Supernovae in Three Dimensions: A Sneak Preview”. In: *Annual Review of Nuclear and Particle Science* 66.1 (Oct. 2016), pp. 341–375. DOI: 10.1146/annurev-nucl-102115-044747. URL: https://doi.org/10.1146%2Fannurev-nucl-102115-044747.

[45] Xing-tao Huang et al. “Offline Data Processing Software for the JUNO Experiment”. In: Feb. 8, 2017, p. 1051. DOI: 10.22323/1.282.1051.

[46] S. Agostinelli et al. “Geant4—a simulation toolkit”. In: *Nuclear Instruments and Methods in Physics Research Section A: Accelerators, Spectrometers, Detectors and Associated Equipment* 506.3 (July 1, 2003), pp. 250–303. ISSN: 0168-9002. DOI: 10.1016/S0168-9002(03)01368-8. URL: https://www.sciencedirect.com/science/article/pii/S0168900203013688.

[47] J. H. Zou et al. “SNiPER: an offline software framework for non-collider physics experiments”. In: *Journal of Physics: Conference Series* 664.7 (Dec. 2015). Publisher: IOP Publishing, p. 072053. ISSN: 1742-6596. DOI: 10.1088/1742-6596/664/7/072053. URL: https://dx.doi.org/10.1088/1742-6596/664/7/072053.

[48] Tao Lin et al. “Simulation software of the JUNO experiment”. In: *The European Physical Journal C* 83.5 (May 2023). DOI: 10.1140/epjc/s10052-023-11514-x. URL: https://doi.org/10.1140%2Fepjc%2Fs10052-023-11514-x.

[49] Angel Abusleme et al. “Calibration strategy of the JUNO experiment”. In: *Journal of High Energy Physics* 2021.3 (Mar. 1, 2021), p. 4. ISSN: 1029-8479. DOI: 10.1007/JHEP03(2021)004. URL: https://doi.org/10.1007/JHEP03(2021)004.

[50] JUNO Offline Group. *JUNO offline user manual (OUM)*. 2012-2023. URL: https://juno.ihep.ac.cn/~offline/Doc/user-guide/index.html.

[51] Guanghua Gong et al. “The Global Trigger with Online Vertex Fitting for Low Energy Neutrino Research”. In: *15th International Conference on Accelerator and Large Experimental Physics Control Systems*. 2015, THHB2O03. DOI: 10.18429/JACoW-ICALEPCS2015-THHB2O03.

[52] Miao Yu. “Progress on NMO Study by Early Supernova Neutrinos”. In: Kaiping: Presentation at the 21st JUNO Collaboration Meeting, Feb. 8, 2023.

[53] Karolina Rozwadowska et al. “On the rate of core collapse supernovae in the milky way”. In: *New Astronomy* 83 (2021), p. 101498. ISSN: 1384-1076. DOI: https://doi.org/10.1016/j.newast.2020.101498. URL: https://www.sciencedirect.com/science/article/pii/S138410762030289X.

[54] Manne Segerlund et al. *Measuring the distance and mass of galactic core-collapse supernovae using neutrinos*. 2021. arXiv: 2101.10624 [astro-ph.HE].

[55] Steve Baker and Robert D. Cousins. “Clarification of the use of CHI-square and likelihood functions in fits to histograms”. In: *Nuclear Instruments and Methods in Physics Research* 221.2 (Apr. 1984), pp. 437–442. ISSN: 01675087. DOI: 10.1016/0167-5087(84)90016-4. URL: https://linkinghub.elsevier.com/retrieve/pii/0167508784900164.

[56] Luca Lista. *Statistical Methods for Data Analysis in Particle Physics*. Vol. 941. Lecture Notes in Physics. Cham: Springer International Publishing, 2017. ISBN: 978-3-319-62839-4 978-3-319-62840-0. DOI: 10.1007/978-3-319-62840-0. URL: https://link.springer.com/10.1007/978-3-319-62840-0.

[57] Jarah Evslin. *Confidence in the neutrino mass hierarchy*. 2013. arXiv: 1310.4007 [hep-ph].

[58] Glen Cowan et al. “Asymptotic formulae for likelihood-based tests of new physics”. In: *The European Physical Journal C* 71.2 (Feb. 2011). DOI: 10.1140/epjc/s10052-011-1554-0. URL: https://doi.org/10.1140%2Fepjc%2Fs10052-011-1554-0.

[59] Mark Thomson. *Graduate lectures on statistics - Chi-squared and likelihood fitting*. University of Cambridge. 2015. URL: https://www.hep.phy.cam.ac.uk/~thomson/lectures/lectures.html.